ADVANCED OPTICAL MATERIALS
www.advopticalmat.de

Up- and Down-Shifting Nanomaterials with Chiroptical Responses: Origin of their Chiroptical Activity and Applications

*Laura Francés-Soriano, Elena Zaballos-García, and Julia Pérez-Prieto**

Artificial chiral nanoparticles exhibit unique optical and (photo)physical properties. They can be all-inorganic or organic–inorganic materials that are usually confined to the nanoscale by anchoring organic ligands to their surface. The ligands can also possess distinctive optical and/or (photo)physical properties, thereby adding functionality to the whole nanosystem and constituting an organic–inorganic nanohybrid. Development of luminescent chiral nanoparticles and nanohybrids is pertinent to many applications, such as (bio)sensing, therapeutics, photocatalysis, and optoelectronics, among others. This review deals with different photoactive nanomaterials, displaying either up-shifting emission (nanoparticles consisting of a photoactive or inert matrix doped with lanthanides, Ln^{3+}, upconversion nanoparticles, UCNPs) or down-shifting emission, such as coinage metal nanoclusters (e.g., gold nanoclusters, AuNCs) and lead halide perovskite nanoparticles (HP NPs), as well as very low emissive nanoparticles, such as plasmonic nanoparticles (such as gold nanoparticles, AuNPs). Special attention is paid to the origin of the chiroptical response of these materials, showing that it is varied and can be alike for some of them.

1. Introduction

The interest of chiral materials is rocketing due to their potential in different fields such as catalysis, (bio)sensing, optics, and photonics, aside from manufacturing of pharmaceutical/chemical products and building materials.[1] Standard analytical techniques used for the characterization of materials, such as absorption, emission and mass spectroscopy, among others, are not able to distinguish between chiral molecules/materials. However, circular dichroism (CD), an absorption spectroscopy, and circularly polarized luminescence (CPL), an emission spectroscopy, are useful techniques for the observation of their chirality.[2] Both CD and CPL use circularly polarized light for investigating structural aspects of optically active chiral media. CD measures the absorption difference between the incident left- and right-handed circularly polarized light and has been widely used in the sensing of chiral molecules.[3]

The chiroptical response of an absorbing medium can be evaluated by the absorptive dissymmetry factor, g_{abs}, see Equation (1), where A_L and A_R are the absorption intensities for left- and right-handed circularly polarized light, respectively.[4]

$$g_{abs} = \frac{2\left(A_L - A_R\right)}{A_L + A_R} \tag{1}$$

The g_{abs} factor enables the quantitative comparison of different chiroptical materials and considers both reflected and transmitted left- and right-handed circular polarized waves. By definition, its value is between −2 to +2 for purely right-handed and purely left-handed circularly polarized light, respectively.[5]

On the other side, CPL determines the different emission of left-circularly and right-circularly polarized light in chiral luminophores and can be quantified by means of the luminescence dissymmetry factor (g_{lum}).[6] Analogously to g_{abs}, g_{lum} is defined as:

$$g_{lum} = \frac{2\left(I_L - I_R\right)}{I_L + I_R} \tag{2}$$

where I_L and I_R are the intensity of the left- and right-circularly polarized emission, respectively. It should be noted that in molecular systems, CD spectrum reflects chirality information about the molecular ground states, whereas CPL spectrum reveals the chiroptical properties of the molecular emitting states.[7]

L. Francés-Soriano, J. Pérez-Prieto
Instituto de Ciencia Molecular (ICMol)
Universitat de Valencia
Calle Catedrático José Beltrán 2, Paterna, Valencia 46980, Spain
E-mail: julia.perez@uv.es
E. Zaballos-García
Department of Organic Chemistry
Universitat de Valencia
Av. Vicent Andrés Estellés s/n, Burjassot, Valencia 46100, Spain

The ORCID identification number(s) for the author(s) of this article can be found under https://doi.org/10.1002/adom.202300337

DOI: 10.1002/adom.202300337

Chirality at the nanoscale can be of great interest due to the potential application of chiral nanomaterials in nanotechnology,[8] catalysis,[9] optical devices,[10] and biomedicine,[11] among others. For example, chirality in nanomaterials can enhance cellular uptake and prolong their in vivo stability in blood, thereby enhancing their therapeutic performance. The cytotoxicity of some chiral nanomaterials can be reduced by their capping with surface ligands.[12] In the case of inorganic nanomaterials, they can exhibit considerable absorption differences on left-handed and right-handed circularly polarized (LCP and RCP) radiations, which can be beneficial in terms of their application in selective therapy. Moreover, altering the chirality of nanoparticles and clusters by means of circularly polarized light can eventually result into self-assembly of the nanoparticles to generate structures with hierarchical chirality.

In general, chiral transfer of photons to racemic nanoparticles has been used for obtaining enantiomeric excess in the chiral synthesis of nanomaterials, e.g., irradiation of racemic cadmium tellurite (CdTe) semiconductor nanoparticles with LCP and RCP light finally induced the formation of left- and right-handed twisted nanoribbons, with an enantiomeric excess exceeding 30%.[13] Racemic CdTe NP colloids containing particles and small clusters illuminated by LCP at 543 nm produced a subpopulation of left-handed nanoparticles and clusters, which absorbed light more effectively than the right-handed nanoparticles and clusters. The same applied to the enantiomeric nanoparticles and nanoclusters when illuminated with RCP light. Excitation of thioglycolic acid (TGA)-stabilized CdTe nanoparticles provoked the photooxidation of the ligands and, therefore, bare core-shell cadmium tellurite/cadmium sulfide (CdTe@CdS) nanoparticles were obtained.[14] In addition, circularly polarized light can also induce the self-assembly of nanoparticles on the basis of the chirality of nanoparticles and cause the magnification of circular polarization effects in nanoparticle assemblies. The chirality of the constituent building blocks, i.e., chiral nanoparticles, is reflected in the helicity of the resulting assemblies, as occurs with the self-assembly of organic and biological macromolecules.[13]

Another example of chiral nanoparticles is that of tellurium nanoparticles (TeNPs). Although tellurium is chiral, since it shares intrinsically chiral space groups, it typically requires chiral stimuli, such as a chiral ligand, to form a chiral shape. Chiral polyhedral TeNPs have recently been prepared by ligand-mediated hydrothermal-assisted synthesis, using an enantiomerically pure cysteine (Cys) to modify the morphology of the nanoparticles, from a two dimensional (2D) shape to a chiral three dimensional (3D) polyhedron, by inducing screw dislocation effects during the nanoparticle growth.[15]

Tellurium precursors were reduced in the presence of large amounts of a Cys enantiomer (*D*-Cys or *L*-Cys), which thiol group strongly bound to tellurium; hydrazine hydrate was added before the rapid reduction of the biomolecule occurred. The growth of the nanoparticle was controlled by using polyvinylpyrrolidone (PVP) under alkaline conditions. **Figure 1** shows the Scanning electron microscopy (SEM) images of chiral TeNPs at different reaction times. After 3 h, overall spherical-shaped crystals started to grow and after eleven hours most of the crystals exhibited chiral shapes. Most of the crystals fully growth after eighteen hours, but only some of them had chiral shapes.

Different photoactive nanomaterials, displaying either up-shifting emission, such as i) nanoparticles with lanthanide (Ln^{3+})-doped (photoactive or inert) matrices, known as upconversion nanoparticles (UCNPs), and ii) down-shifting emission, such as coinage metal nanoclusters (e.g., gold nanocluster, AuNCs) and lead halide perovskite nanoparticles (HP NPs), as well as very low emissive nanoparticles, such as plasmonic nanoparticles (gold nanoparticles, AuNPs), can present a chiroptical response. The origin of such response can be alike for the different materials (**Figure 2**): i) intrinsic chirality due to chiral lattice distortions and defects, ii) chiral interactions between achiral and chiral nanoparticles, iii) assembling of chiral nanostructures of achiral NPs. Precisely controlled chiral nanomaterials can be achieved by means of chiral self-sorting, a phenomenon wherein racemic components are spontaneously arranged into homo- or heterochiral molecular assemblies through chiral discrimination between the components,[16] the majority-rules effect by using a slight excess of one enantiomer to lead to a strong preference toward the helical sense preferred by the enantiomer that is present in majority,[17] and a chiral environment or stimuli.

We will focus here on the origin of the chiroptical response of nanomaterials which differ in their composition and optical properties; in particular, UCNPs, AuNPs, AuNCs and lHP NPs. For extended information about these or other nanomaterials, as well as nanoassemblies, the authors address the readers to recent reviews.[18–20]

2. Chiroptical Response in Gold Nanoclusters

Gold nanoclusters are small-sized nanoparticles (< 3 nm, several tens of gold atoms), which exhibit a good photostability, considerable Stokes-shifted emission and inherent good biocompatibility.[21] Depending on the nature of the capping ligand, in particular the ligand anchoring group(s), the nanoclusters can absorb in the UV–vis region or in the UV-near infrared I (NIR-I) region. In the case of thiolate-protected AuNCs, they typically consist of a metal core with Au–Au bonds (≈2.8 Å) and surface Au–S staple motifs.[22]

In terms of their photoluminescence (PL), bare AuNCs are not emissive, while capping of their surface with organic ligands can convert them into nanofuorophores. AuNCs usually emit in the VIS region, but can emit in the VIS-to-NIR II region when they are capped with thiolate ligands.[23] The nanoclusters can be prepared by either a top-down strategy consisting of etching AuNPs[24,25] or by a bottom-up strategy consisting of reducing $HAuCl_4$ in the presence of a reduction agent and stabilizer, such as thiols (e.g., cysteine, glutathione), amines (e.g., polyamidoamines) and Good's buffers (e.g., N-(2-hydroxyethyl)piperazine-N'-(2-ethanesulfonic acid, HEPES), among others.[26]

Nanocluster functionality can be enhanced by incorporating ligands of relevant functionality, such as flavine adenine dinucleotide (FAD) cofactor, with a strong absorption in the blue and violet wavelength region (peak maximum at 460 and 370 nm, respectively) compared to the small absorption of the AuNC in the UV region and the even weaker absorption in the visible region.[27] Sensitized emission (λ_{ex} = 390 nm) of FAD by AuNC in FAD-capped AuNCs (AuNC@FAD) nanohybrids occurred

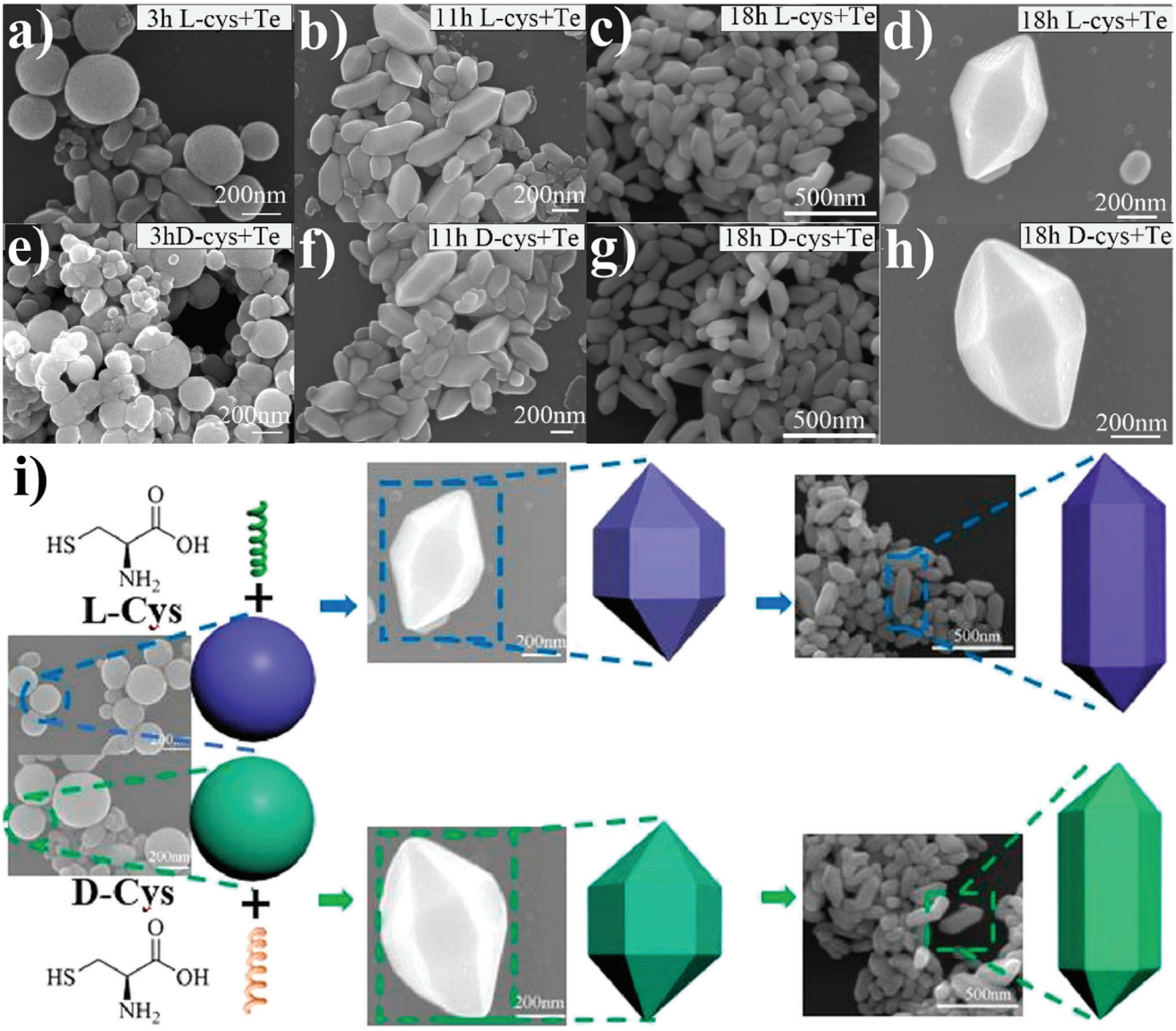

Figure 1. Scanning electron microscopy (SEM) images of chiral tellurium nanoparticles (TeNPs) upon reaction with *L*-Cys and *D*-Cys at different reaction times (3–18 h); a,c,e) *L*-Cys, 3, 11, and 18 h, respectively; b,d,f) D-Cys, 3, 11, and 18 h, respectively. g,h) show the *L*-Cys and *D*-Cys chiral shapes of TeNPs, respectively. i) Schematic mechanism of the formation of chiral polyhedral TeNPs by using *L*- and *D*-cysteine enantiomers and circular dichroism spectra of the NPs. Adapted with permission.[15] Copyright 2022, American Chemical Society.

because of the overlap between the AuNC fluorescence and FAD absorption.

Many metal nanoclusters exhibit chirality reflected by their chiroptical activity in metal-based electronic transitions (**Figure 3**a–c).[28] Discrete chiroptical activity can arise from the intrinsically chiral inorganic core because their shapes are not completely symmetrical (owing to dislocations and vacancies, among others).[29] Such cores are considered as minimum energy geometries for various clusters,[30] such as coordination chiral clusters[31] and bare metal clusters.[32–35]

Moreover, a chiral organic shell can produce chiroptical activity on achiral cores when using an enantiomerically pure ligand, such as *N*-acetyl-*L*-cysteine, which possesses a strong coordinating group, specifically a mercapto group, aside from the carboxylic group,[36] and bicyclic thiolates, among others.[37] In addition, chiral ligands can anchor to an achiral core surface through at least two points, thus creating a chiral footprint, e.g., the bidentate feature of 1,2-bis(diphenylphosphino)ethane (dppe) ligands has led to propeller-like structures, thereby reducing the symmetry of the AuNC to C1.[38] Simulated electronic CD spectrum evidenced the generation of $[Au_{13}(dppe)_5Cl_2]^{3+}$ NCs, a chiral ansa metallamacrocycle which exhibits near-infrared photoluminescence and can produce singlet oxygen ($^1O_2$) with a considerable high yield (up to 0.71).[38]

Moreover, the use of binary mixed ligands of chiral and achiral diphosphines, such as 2,3-O-isopropylidene-2,3-dihydroxy-1,

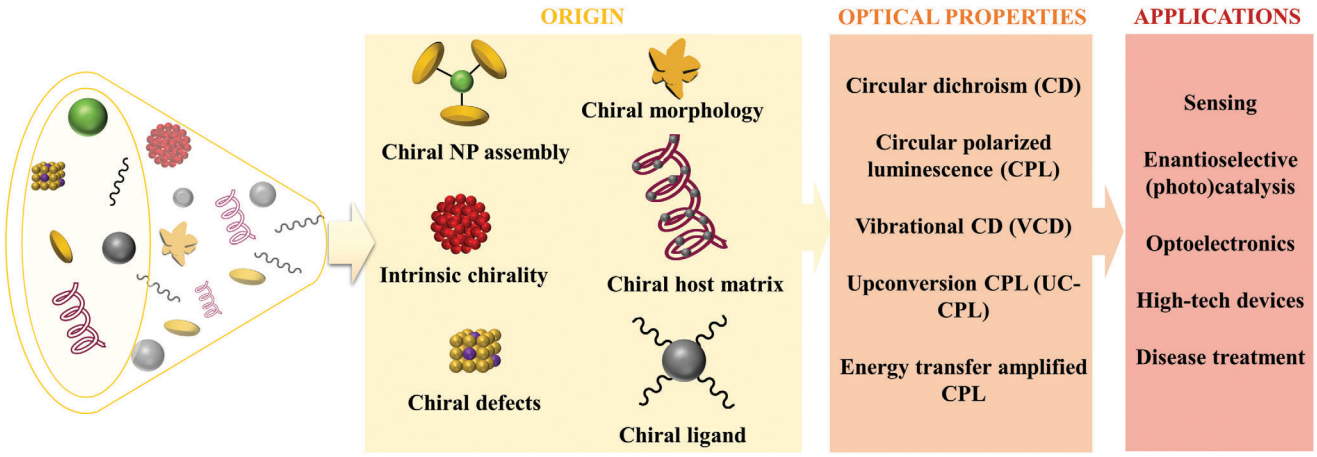

Figure 2. Overview of the chiral origin of inorganic nanoparticles and their chiroptical properties and further applications.

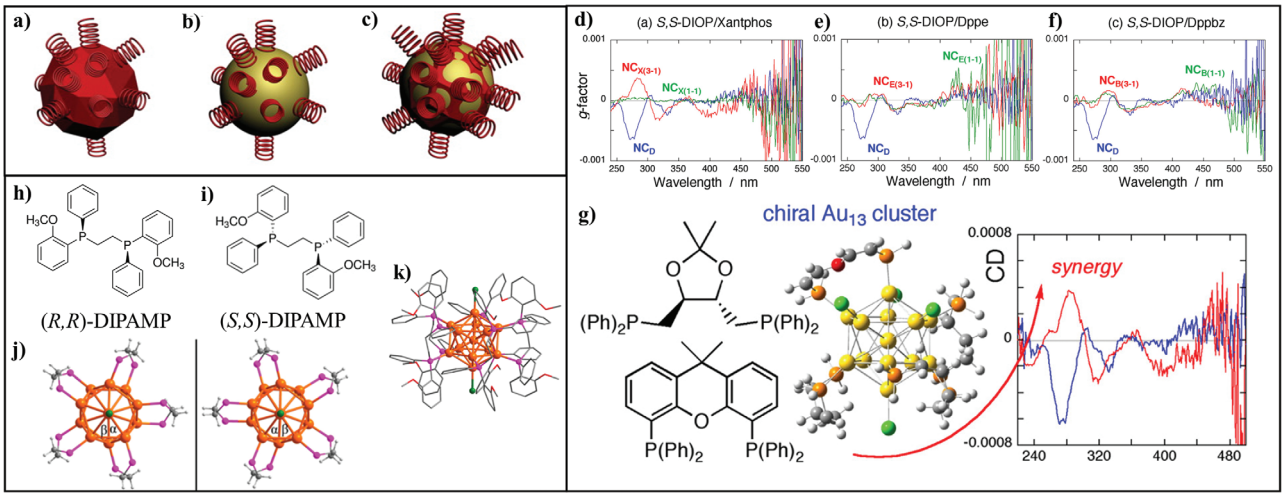

Figure 3. a–c) Scheme of the origins of optical activity in metal particles with individual chirality: a) intrinsically chirality, b) chiral distribution of NP electron density induced by molecular chiral ligands and c) chiral footprint on the NP surface. Adapted with permission.[29] Copyright 2011, Elsevier Ltd. d–f) Calculated g_{abs}-factors of Au_{13}NCs: d) $NC_{Xantphos/DIOP(3-1)}$ or $NC_{Xantphos/DIOP\ (1-1)}$, e) $NC_{Dppe/DIOP\ (3-1)}$ or $NC_{Dppe/DIOP(1-1)}$, and f) $NC_{Dppbz/DIOP\ (3-1)}$ or $NC_{Dppbz/DIOP(1-1)}$. The blue line corresponds to the g_{abs}-factor of samples capped only with the chiral ligand (1*S*,1*S*)-DIOP. g) Structure of (1*S*,1*S*)-DIOP (left-up), Xantphos (left-bottom), and the Au_{13}NCs capped with DIOP and Xantphos (center) and its CD spectrum (right). Adapted with permission.[39] Copyright 2020, American Chemical Society. Structure of the h) (*R*,*R*)-DIPAMP ligand, i) (*S*,*S*)-DIPAMP ligand, and k) cation part of Au_{13}NC@(*R*,*R*)-DIPAMP. j) Top view of the core structures of Au_{13}NC@(*R*,*R*)-DIPAMP (left) and Au_{13}NC@(*S*,*S*)-DIPAMP (right). Adapted with permission.[41] Copyright 2019, American Chemical Society.

4-bis(diphenylphosphino)butane, (*S*,*S*)-DIOP, chiral diphosphine, and the achiral diphosphine 4,5-bis(diphenylphosphino)-9,9-dimethylxanthene (Xantphos), has produced Au_{13}NCs with chiroptical activity.[39] Testing different chiral/achiral ligands ratio (specifically, 1/0, 3/1, or 1/1 ratios) demonstrated that a 3/1 (*S*,*S*)-DIOP/Xantphos ratio provided a higher chiroptical activity than pure (*S*,*S*)-DIOP in a core-based transition region (Figure 3d–g).

To gain insight into the synergetic effect between the chiral and achiral ligands in the chiroptical response of the AuNCs, quantum chemical calculations and geometrical quantifications based on the Hausdorff chirality measure (HCM),[40] which quantifies the chirality of a geometric representation of an object by measuring the degree of coincidence of the object with its mirror image, have been carried out using model Au_{13}NCs. Data suggest that the chiroptical enhancement can be due both to the effect of limited isomer configurations and larger HCM values compared to that of the cluster passivated with the pure chiral diphosphine.

Furthermore, Zhan et al.[41] foresaw the requisite of the stereogenic moiety to be close to the ligand backbone for a successful enantioselective preparation of a pair of enantiopure Au_{13}NCs. To this aim, they selected 1,2-bis[(2-methoxyphenyl)phenylphosphino]ethane (DIPAMP), with stereogenic centers at the phosphorus atoms due to the asymmetric attachment of the methoxyl groups. The helical arrangement of the ligand produced distorted icosahedral cores, thereby accounting for their chiroptical activity in the VIS. The chiral configuration of the nanocluster was controlled by the chirality

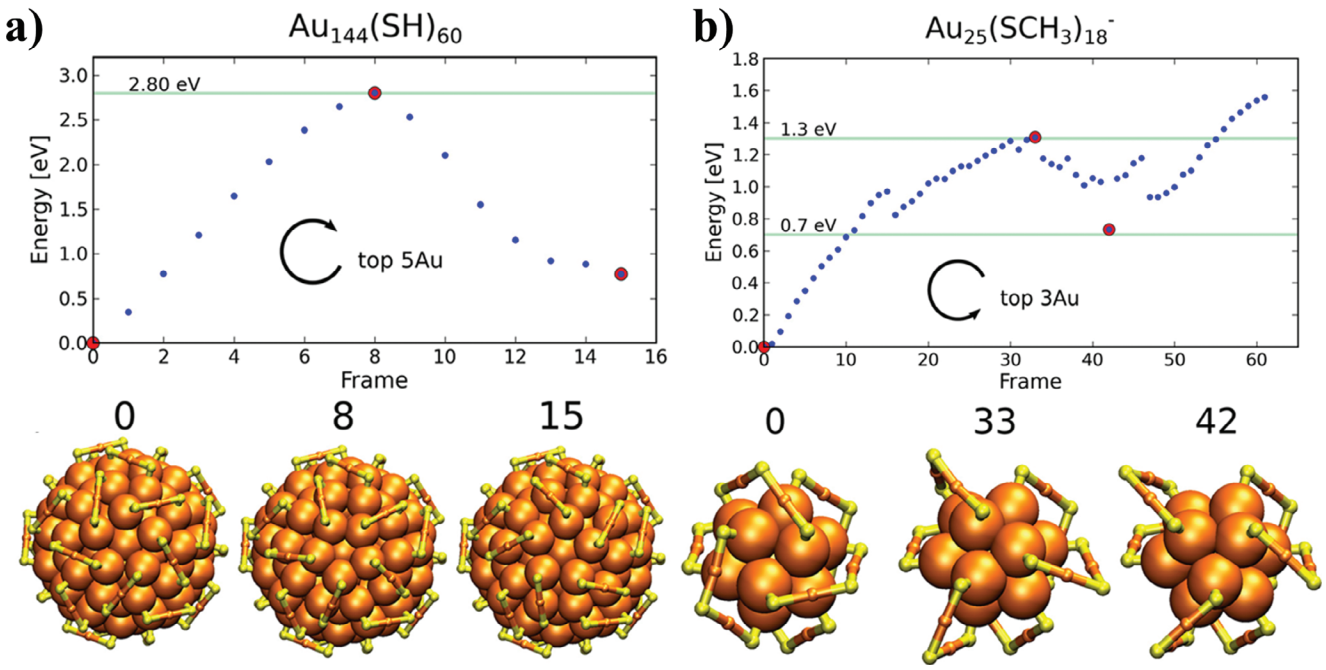

Figure 4. a) Inversion energy profile and selected configurations of $Au_{144}NC(@(SH)_{60}$ by rotation of the five core Au atoms closest to the C_5 symmetry axis parallel to the top view direction. Plot of the energy as a function of reaction frame (top) and the selected frames corresponding to red data points in the graph (bottom). Only the gold–sulfur framework is shown for clarity. The arrow in panel a (top) denotes the direction of the rotation. b) Transformation of $[Au_{25}NC@(SCH_3)_{18}]^-$ by rotation of the three core Au atoms closest to the C_3 symmetry axis. Energy profile (top) and selected structures corresponding to red data points in panel b (bottom). Only the gold–sulfur framework is shown for clarity. The arrow in panel a (top) denotes the direction of the rotation. Adapted with permission.[46] Copyright 2019, American Chemical Society.

of the diphosphine ligand, the right-handed cluster was obtained when using *(R,R)*-DIPAMP, *(R,R)*-DIPAMP, while the left-handed one resulted from the *(S,S)*-DIPAMP (Figure 3h–k).

Among the strategies for the synthesis of chiral metal clusters are i) a spontaneous process of symmetry breaking, by which a physical system in a symmetric state spontaneously ends up in an asymmetric state (spontaneous symmetry breaking); ii) direct asymmetric synthesis by using a chiral reagent (chiral ligands induction; chiral precursor induction; chiral reducing agent induction; chiral counterions induction); iii) achiral-to-chiral transformations; and iv) manipulation of chiroptical activity (heterometal doping, surface-structure modulation, aggregation, or assembly).[42] Thus, spontaneous symmetry breaking can consist in the use of multidentate ligands to increase the probability of forming a chiral network on the cluster surface compared to monodentate ligands.

Chiral ligands induction is based on chiral ligands which coordinate to metals at the NC surface, therefore, the chirality from ligands can be transferred inside the metal interface and even the core, thus inducing asymmetric arrangement of the metal framework. In addition, chiral clusters can be produced by using chiral precursors and chiral reducing agents. Chiroptical activity can be induced upon the addition of non-coordinating chiral ions and chiral solvent, which can tailor the structure and regulate the chiroptical properties of clusters by directional intermolecular hydrogen bonding, electrostatic attraction, and steric effect. Moreover, achiral-to-chiral transformations are based on symmetry-breaking of specific metal cluster by substituting the weak coordinated sites with chiral ligands.

Moreover, transfer of the chirality can occur from a AuNC to an achiral molecule adsorbed on its surface.[43] Thus, solutions of chiral $Au_{38}NC@(2\text{-PET})_{24}$ cluster enantiomers, where PET was 2-phenylethylthiolate molecules, showed strong vibrational circular dichroism (VCD) signals in vibrations of the achiral PET. Density functional theory (DFT) calculations revealed that 2-PET molecules adopt a chiral conformation. Chirality transfer from the cluster to the achiral ligand was responsible for the preference of one of the two enantiomers. Intermolecular interactions between the ligands on a crowded cluster surface seem to play a dominant role in chirality transfer from metals to ligands and this phenomenon could play an important role in heterogeneous enantioselective catalysis.

In addition, the enantio-enrichment of a chiral cluster can be addressed by using chiral high-performance liquid chromatography (HPLC) or deracemization, a method for the selective separation of a racemic mixture based on the use of a chiral stationary phase. For example, a chiral cellulose-based analytical HPLC column interacted differently with the left- and right-handed $Au_{38}NC@(2\text{-PET})_{24}$, thereby providing an enantiomerically enriched mixture.[44]

Remarkably, chiral inversion of thiolate-capped AuNCs has shown to be sensitive to the size, structure and metal composition of the metal core, as well as to the structure of the metal–thiolate interface (**Figure 4**).[45,46] Some of them, such as chiral $Au_{38}NC@(SR)_{24}$, can tolerate chiral inversion without requiring the breakage of a metal–sulfur bond at the metal–ligand interface, but undergoes a collective rotation of the gold core (the calculated energy barrier for $Au_{38}NC$ was in the range of 1–1.5 eV,

compared to 2.5 eV for the of Au−S bond cleavage). $Au_{38}(SR)_{24}$ and $Au_{25}NC(SR)^{18-}$ have an icosahedral core but the first consists of only one Au_{13} icosahedron, while the second presents a face-fused bi-icosahedron. The arrangement of the protecting units is partly analogous to that of $Au_{38}NC(SR)_{24}$, with the same rotational reconstruction mechanism than $Au_{38}NC(SR)$ and a low energy barrier (1.30 eV).

However, inversion barriers are much higher (2.5−2.8 eV) for a larger chiral nanocluster, such as $Au_{144}NC@(SR)_{60}$; this makes these NCs promising materials for applications requiring high resistance to chiral inversion.[46]

Regarding applications of AuNCs, it has been reported that nanoclusters protected with *L*- and *D*-penicillamine exhibit mirror-image CD in the 200–400 nm absorption region.[47] The biocompatibility of the AuNCs together with their photostability and fluorescence emission at 630 nm make them of interest in optical imaging of live HeLa cells using confocal microscopy.

Moreover, co-assembling of achiral thiobarbituric acid (TBA)-capped AuNCs with enantiomerically pure (*L*- or *D*-)-histidine (His) has provided hydrogels, denoted as *L*-gels and *D*-gels, generated via H-bonding and π–π stacking between TBA and the corresponding histidine.[48] DFT calculations revealed a parallel conjugated structure of TBA and His at 3.358 Å, thus strongly supporting the π–π stacking between TBA and histidine. The gelation and chirality transfer proved to be essential for their selective generation and for the enhanced emission of the hydrogels, which exhibit a twisty peanut-like structure and represent novel chiroptical materials.

Additionally, AuNCs functionalized with axially chiral binaphthyls (either in the cisoid or transoid conformation) have been exploited as additives in achiral liquid crystal (LC) phase to generate a chiral nematic LC phase.[49]

3. Chiroptical Response in Lead Halide Perovskites

Lead HPs exhibit exceptional optoelectronic properties, such as high absorption coefficient, low non-radiative recombination rate, high photoluminescence quantum yield, and long carrier lifetime.[50] They can present a three-, two-, one-, or zero-dimensional framework (3D, 2D, 1D or 0D).[51] The general chemical formula for 3D metal halide perovskites is AMX_3, where A represents a monovalent cation (organic or inorganic cation) and M and X represent a metallic cation and halogenic anion, respectively.[52] Those with A being an organic cation are known as hybrid organic–inorganic perovskites (HOIPs), while those with A being an inorganic cation are known as all-inorganic perovskites (IPs). Corner-shared $[MX_6]$ octahedrons form a 3D framework with A cation located in the framework cavities.[53] 3D lead HPs exhibit long carrier-diffusion lengths, high carrier mobilities, high dielectric constants, low trap densities and tuneable bandgaps.

Building of stable 3D chiral IP NPs has shown quite difficult to achieve.[54] Both HOIPs and IPs can constitute chiral perovskites via different approaches.[55] Chirality transfer to a perovskite nanoparticle can occur via similar strategies to those mentioned above for other materials, such as i) nanoparticle surface distortion caused by anchoring of chiral ligands, ii) interaction between achiral and chiral systems, iii) supramolecular chiral self-assembly and iv) mediated by chiral molecules.

Nanoparticle surface distortion caused by the interaction between chiral organic molecules or capping agents and core materials, such as quantum dots (QDs) or metal nanoparticles, has also been observed in chiral HOIPs.

Focusing on all-inorganic chiral perovskite NCs, $CsPb(I/Br)_3$ nanoparticles decorated with a chiral ligand, such as 1,2-diaminocyclohexane, DACH, enantiomers, have been prepared by addition of $CsPb(I/Br)_3$ nanocrystals capped with oleylamine (OA) to a mixture of chiral DACH, either (1*R*,2*R*)-DACH or (1*S*,2*S*)-DACH, in n-hexane to $CsPb(I/Br)_3$. Then, they were exposed to microwave irradiation to induce spontaneous ligand exchange from the achiral capping agent OA to the chiral stabilizer.[56] The chiral $CsPb(I/Br)_3$@(1*R*, 2*R*)-DACH and $CsPb(I/Br)_3$@(1*S*, 2*S*)-DACH nanocrystals exhibited chiroptical activity as demonstrated by CD spectroscopy. $CsPb(I/Br)_3$@(1*R*, 2*R*)-DACH nanocrystals displayed two negative Cotton effects at 290 and 400 nm along with a positive CD signal at 333 nm. Comparatively, the CD spectrum of pure (1*R*,2*R*)-DACH stabilizer only exhibited a positive Cotton effect at a shorter wavelength (233 nm), thus confirming that the Cotton effect originated from the chirality of the nanocrystals. Remarkably, the chiroptical activity of $CsPb(I/Br)_3$ remained unchanged even after the removal of chiral molecules.

Moreover, Chen et al. addressed the synthesis of chiral $CsPbBr_3$ colloids via a direct growth of perovskite nanocrystals in the presence of precursors and chiral molecules; specifically, *(R)*- or *(S)*-α-octylamine was used as the chiral capping ligand.[57] The CD spectra showed mirror images of the signal at 504 nm attributed to the exciton absorption; this was consistent with the interaction between chiral α-octylamines and the nanocrystal surface. CPL spectroscopy showed signals of the chiral nanoparticle at $\approx$ 525 nm. An excess of bromide atoms on the nanoparticle surface enabled selective chiral amine binding to Br-rich defect sites, thus resulting in a distorted surface pattern on the nanocrystal. **Figure 5**a shows the interaction of the material with chiral organic molecules; the electronic interactions between chiral ligands and the achiral inorganic structure; the chiral distortion of the surfaces, induced by chiral organic molecules; and the surface enantiomeric chiral distortions.

The instability of 3D chiral HOIPs (Figure 5b) hinders their practical optoelectronic applicability. Regarding low-dimensional 2D and quasi-2D chiral HOIPs (Figure 5c), they have the $(RNH_3)_2A_{n-1}MX_{3n+1}$ formula, where n is the number of inorganic layers between two layers of organic cations ($n = 1$ and $n > 1$ corresponds to 2D HOIPs and quasi-2D HOIPs, respectively) and RNH_3 is a chiral ligand inserted between two inorganic layers. Moreover, 1D chiral HOIPs (Figure 5d) with the RNH_3MX_3 formula can be generated when chiral organic alkylammonium cations and metallic cations are in a 1:1 ratio. Moreover, a chiral molecule can transfer its chirality to an achiral HOIP nanoparticle, Figure 5e. Remarkably, the incorporation of simple and easily accessible chiral amino acids, such as α-alanine, has been incorporated as a cationic part, so providing chiral HOIPs.[58]

With respect to 2D chiral HOIPs, Lee et al.[59] have recently reported on the incorporation of urea (a non-volatile Lewis base) into the lattice of the perovskite to improve their chiroptical activity, aside from charge transport along the out-of-plane direction (**Figure 6**). The chiroptical activity of the HOIPs has been explained by a stacking conformational change of the benzyl groups

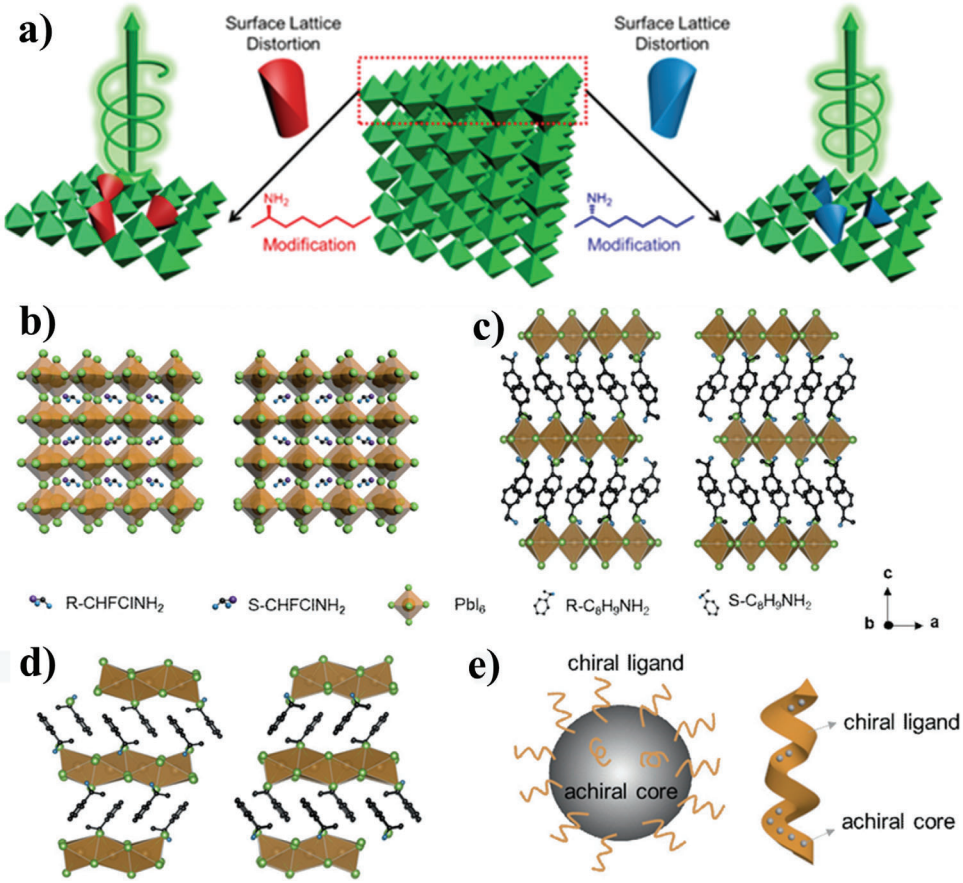

Figure 5. a) Schematic illustration of the origin of chirality in chiral $CsPbBr_3$ perovskite (*R*)- and (*S*)-α-octylamine could induce an asymmetric distortion of the surface perovskite lattice, which endows the chirality to perovskite nanocrystals. Reproduced with permission.[57] Copyright 2019, American Chemical Society. b–d) Representation of the structures of chiral perovskites: b) 3D chiral HOIPS, c) 2D chiral HOIPs, d) 1D chiral HOIPs. e) Representation of assembled chiral perovskites. Adapted with permission.[55] Copyright 2021, Wiley-VCH GmbH.

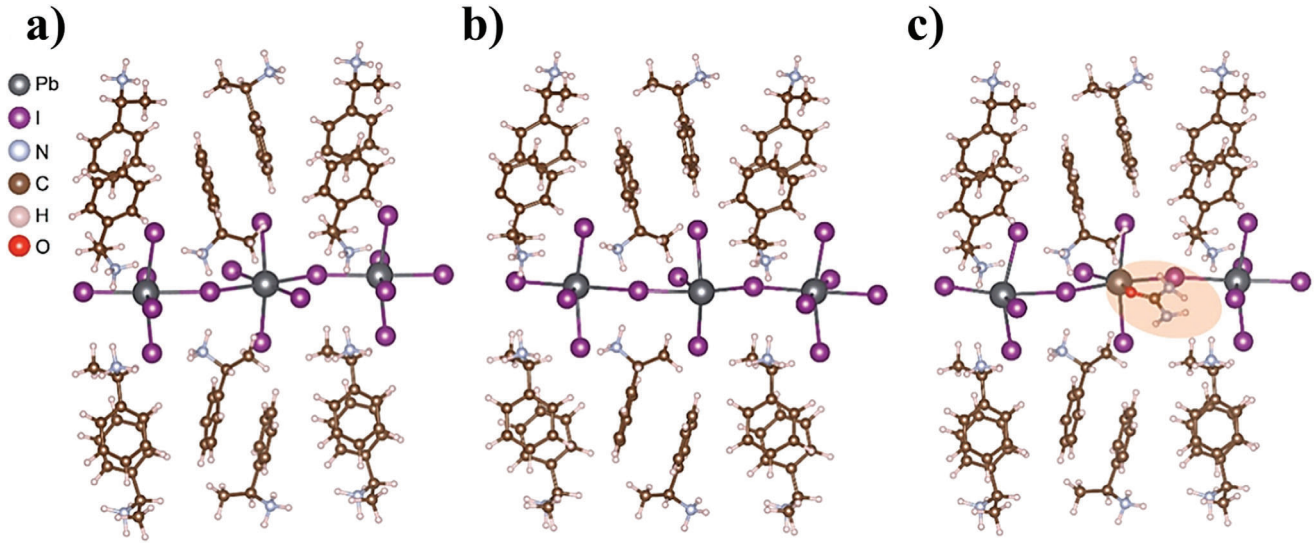

Figure 6. Schematic illustration of the optimized crystal structures: a) without halide vacancy, b) with halide vacancy, and c) in the presence of Lewis base urea at the substitutional site at halide vacancy near the alkyl group of the MBA cation. Adapted with permission.[59] Copyright 2022, American Chemical Society.

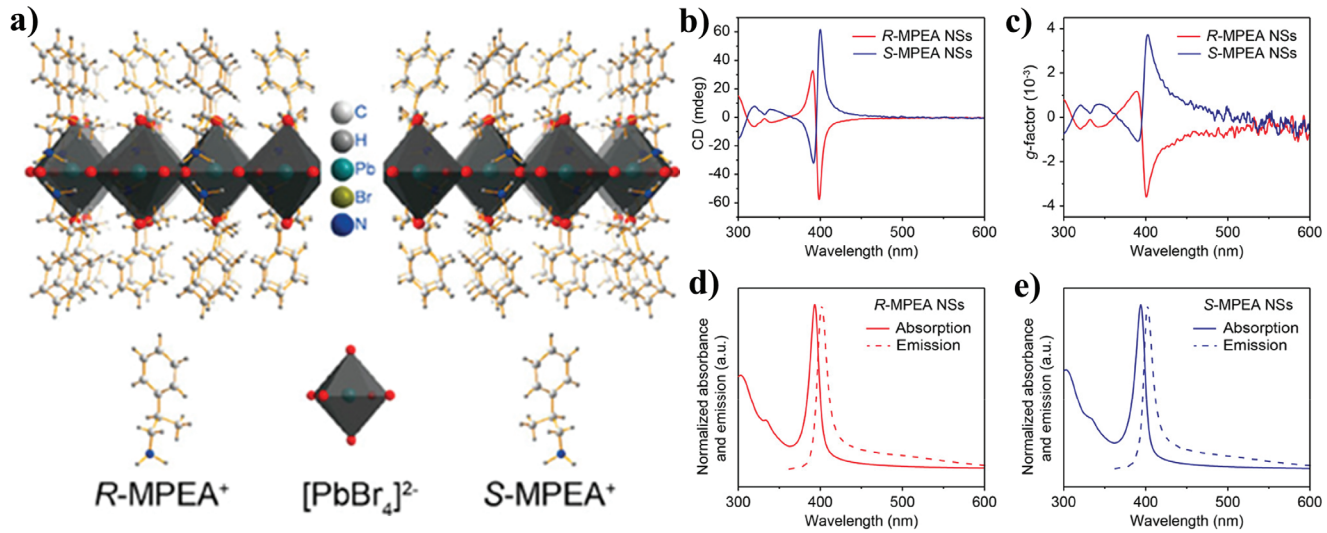

Figure 7. a) Schemes of perovskite nanosheet structure with *(R)*- or *(S)*-MPEA amines ligands. b) CD spectra and c) g_{abs}-factors of chiral MPEA perovskite nanosheets ($n = 1$). d) Absorption (solid line) and emission (dashed line) spectra of *(R)*-MPEA perovskite nanosheets. e) Absorption (solid line) and emission (dashed line) spectra *(S)*-MPEA perovskite nanosheets. Adapted with permission.[60] Copyright 2021, American Chemical Society.

of (*R*)- or (*S*)-methylbenzylamine, (*R*)- or (*S*)-MBA, cations between the inorganic layers. The effect of the Lewis base on the chiroptical activity of the HOIPs was quantified by determining the g_{abs}-factor, obtaining an almost two-fold increase value of CD near the first extinction band edge (a g_{abs}-factor of 1.0×10^{-3} for chiral HOIPs with urea (Figure 6c) versus 5.7×10^{-4} for chiral HOIPs with DMSO only).

Interestingly, it has been demonstrated that chiral *α*-octylamine-capped $CsPbBr_3$ NCs exhibit two-photon absorption-based upconverted circularly polarized luminescence (TP-UC-CPL) with a two-photon absorption cross section at 800 nm ($\sigma_{2800\,nm}$) up to 3.68×10^4 GM.[57] The TP-UC-CPL sense can be selected with the chirality of the capping ligands and the mirror-imaged CPL can be obtained. This is a relevant result from the point of view of designing UC-CPL processes.

Moreover, intrinsically chiral 2D perovskite nanosheets have been obtained by inserting low steric hindrance chiral amines, specifically (*R*)- or (*S*)-*β*-methylphenethylamine, (*R*)- or (*S*)-MPEA, into the perovskite framework, thereby the amine chirality was transferred to the perovskite structure (**Figure 7**).[60] Achiral octylamine protecting the nanosheet influenced considerably the chiral optical signal or dissymmetric factor of the nanosheets; strong CD signals between 375 and 425 nm correspond to the excitonic absorbance band (Figure 7b). The structural flexibility of HOIPs has also enabled the penetration of chiral molecules into its lattice to form inherent chiral crystals.

Chirality generation can also be achieved by introducing chiral molecules, such as a DACH enantiomer, on perovskite NCs stabilized by an achiral ligand.[56] The aggregation of DACH on the surface in a chiral pattern contributes to the chiroptical response of the perovskite NCs mainly caused by two different mechanisms: the chiral surface distortions and chiroptical effects induced by electronic interactions between the ligand and the NCs.

With regards to applications of chiral HOIPs, among others, they are promising ferroelectric materials, e.g., a chiral switchable photovoltaic ferroelectric 1D perovskite [(*R*)- and (*S*)-cyclohexylethylammonium]PbI_3 was achieved by using PbI_6 octahedra and the pair of enantiomeric ligands to induce chirality and ferroelectricity.[61] In addition, optoelectronic devices based on chiral 2D HOIPs [(*S*)- and (*R*)- (methylbenzylamine)]$_2PbI_4$ have shown spin-dependent photovoltaic and photogalvanic responses.[62]

4. Chiroptical Response in Gold Nanoparticles

Plasmonic nanoparticles, such as AuNPs, present characteristic, high absorption peak(s) due to the surface plasmon resonance (SPR) phenomenon that occurs when an electromagnetic radiation, of a wavelength much larger than the diameter of the AuNPs, hits the particles, thereby inducing coherent, resonant oscillations of the metal-free electrons across the nanoparticles. Depending on their shape, the colloid can exhibit one or several SPR peaks at different wavelengths within the UV–Vis–NIR region and, consequently, a distinctive color (**Figure 8**).[63–65]

Plasmonic gold nanoparticles with different sizes and morphologies can exhibit structural or induced CD response.[66] The mechanism of the induced CD is the dipole–plasmon Coulomb interactions between the AuNPs and chiral molecules (**Figure 9**a).[67] Due to the plasmon-enhancement, AuNPs are able to enhance the natural CD lines of the molecules which enable the transfer of molecular chirality to AuNPs, and display chiral response at the plasmon wavelength region. Usually, the induced chirality in AuNPs is responsive to the orientation of the ligands on the AuNP surface and strongly dependent on the overlap between the chiral ligand absorption and plasmon band of the AuNPs.[68] Thus, the absolute value of the g_{abs}-factor is usually small ($\approx 10^{-3}$).

Notably, Fan and Govorov reported a theoretical mechanism of intrinsically optical chirality for single AuNPs with the chiral shapes shown in Figure 9b.[69] The CD response was caused by a

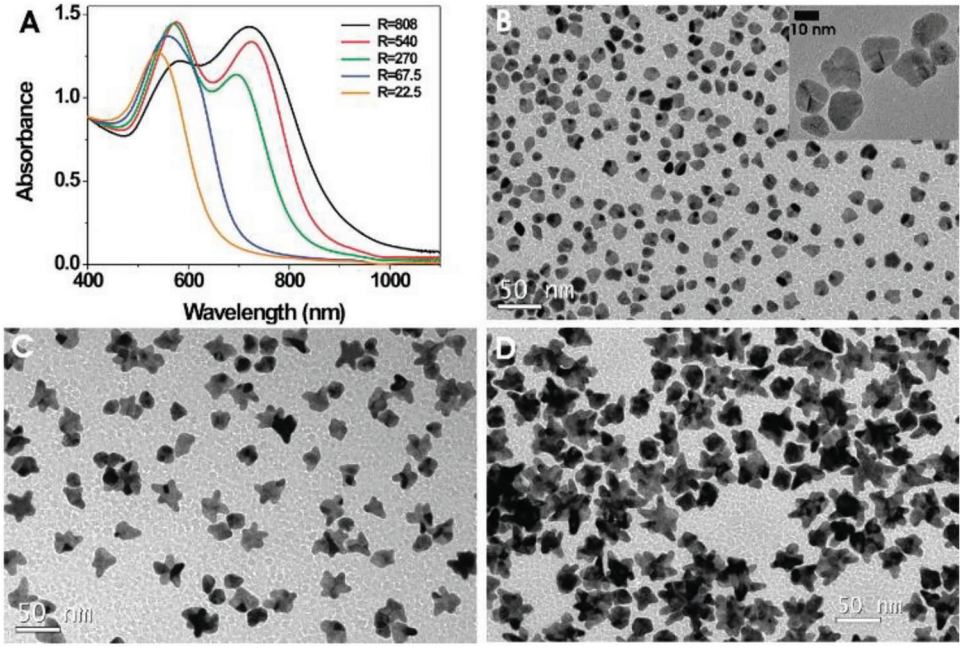

Figure 8. A) Vis–NIR spectra of Au nanostars obtained for different Au salt/Au seed ratio concentrations, using 2.5 nm Au nanoparticles as seeds. B–D) Corresponding TEM images of samples with concentration ratio values of B) 67.5, C) 270, and D) 808. Reproduced with permission.[65] Copyright 2010, American Chemical Society.

chiral distortion of the AuNP surface that originates by both splitting and mixing of plasmonic modes. The largest CD response at the plasmon frequency was observed in twisted and helical distortions (the middle two shapes in Figure 9b).

Moreover, chiral response in AuNPs can be achieved through enantioselective interactions between the chiral planes of the AuNP surface and the chiral ligand, e.g., *L*-Cys and *D*-Cys.[70] These interactions led to different growth rates and the formation of helicoid morphologies with highly twisted chiral elements (Figure 9c). As shown in Figure 9d, the chiroptical responses of helicoids synthesized with *D*- and *L*-Cys displayed opposite handedness.

In addition, 3D chiral AuNPs have been prepared by a seed-mediated growth strategy using octahedral AuNPs as seeds and chiral dipeptides as structure-directing agents to provide chiral morphologies through the extension of crystal facets with a degree of chirality.[71] Relatively similar dipeptides, specifically γ-glutamylcysteine (γ-Glu-Cys) and cysteinylglycine (Cys-Gly) dipeptides, resulted in large morphological differences; the morphology of the γ-Glu-Cys-directed AuNPs showed a cube-like outline with protruded chiral wings with a fourfold symmetry (Figure 9e) However, those synthesized in the presence of Cys-Gly exhibited a rhombic dodecahedron-like outline with curved edges and elliptical cavities on each face (Figure 9f). Therefore, the two types of AuNPs differed in their chiroptic CD response (γ-Glu-Cys led to a positive main peak, while it was negative for Cys-Gly).

Despite the excellent chiroptic response of AuNPs, their potential is limited by its overall synthetic uniformity. Nam et al.,[72] have developed a multi-chirality-evolution step synthesis strategy for enhancing their chiroptic response by increasing the particle uniformity. This strategy has enabled the preparation of chiral nanoparticles with a g_{abs}-factor of 0.31.

Interestingly, the chiral morphology of AuNPs termed nano-octopods has been modulated by using glutathione (GSH) with different degree of oligomerization, thus providing propeller- or flower-like chiral nanoparticles by adjusting the degree of oligomerization of the Au–GSH complexes.[73] The bent arms of de nanoparticles obtained with less GSH oligomers showed two bisignate CD waves assigned to their transverse surface plasmon resonance (TSPR) and longitudinal (LSPR) surface bands of the extinction spectrum. Comparatively, the twisted concaves of the flower-like nanoparticles were obtained when they were prepared with more GSH oligomers and they exhibited a broad bisignate CD wave in the SPR region (**Figure 10**) and maximum g_{abs}-factor of about 0.003 at 830 nm.

Alternatively, discrete chiral plasmonic nanoparticles can consist of metal-molecule-metal nanoparticles (3M NPs, **Figure 11**).[74] They usually contain chiral molecules inside nanogaps or nanocavities between a metal core and an outer metal shell. These chiral molecules must i) contain functional groups which strongly anchor to the seed surface and ii) enable subsequent trapping during metal overgrowth. Chiral biomolecules, such as peptides and DNA have been used with this purpose. The efficiency on the chiral molecule adsorption on the seed surface depends on the crystalline structure and morphology of the metal seed, the concentration of chiral molecules, the bonding strength to different crystal facets, among others. Therefore, the final nanostructure involves a metal–molecule–metal core–shell–shell configuration, in which the chiral molecules constitute the inner shell and/or are embedded in the outer metal shell. The coupling of chiral dipoles from

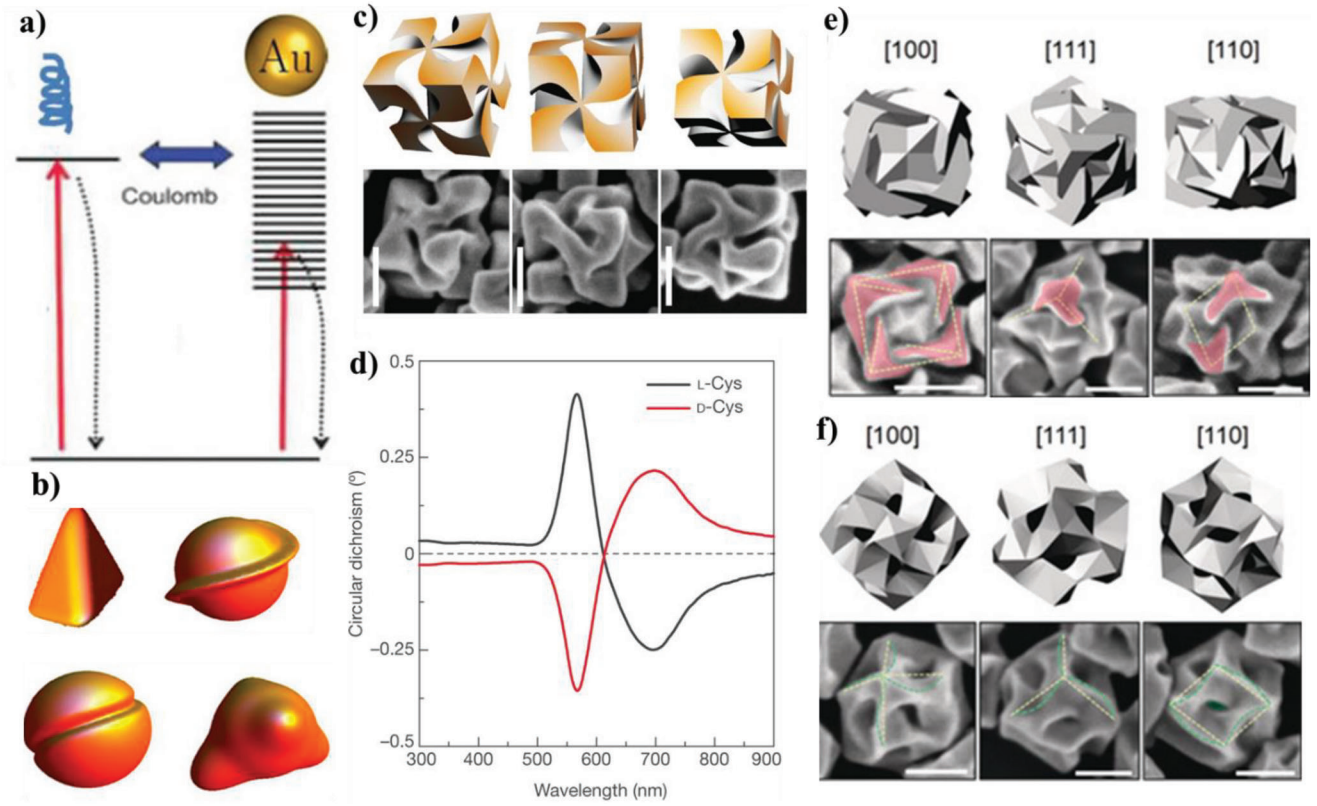

Figure 9. a) Model of exciton-plasmon interaction in a chiral molecule and a AuNP, which generates induced CD; the solid vertical (horizontal) arrows represent light (Coulomb)-induced transitions. The dotted vertical arrows are the relaxation processes. Adapted with permission.[66] Copyright 2019, Wiley-VCH. b) Illustration of different chiral plasmonic nanocrystals with chiral shapes. Adapted with permission.[69] Copyright 2012. American Chemical Society. c) Morphology (top) and SEM image (bottom) of helicoid AuNPs oriented in different directions. Scale bar: 100 nm. Adapted with permission.[70] Copyright 2018, Springer Nature. d) CD responses of helicoids with opposite handedness controlled by cysteine-guided chiral growth. Adapted with permission.[70] Copyright 2018, Springer Nature. e) Structure illustrations and their SEM images of γ-Glu-Cys-directed AuNPs at various directions views: [100] (left), [111] (middle), and [110] (right). Scale bar: 100 nm. f) Structure illustrations and their corresponding SEM images of Cys-Gly -directed AuNPs at different directions views: [100] (left), [111] (middle), and [110] (right). Scale bar: 100 nm. Adapted with permission.[71] Copyright 2020, Wiley-VCH.

the molecule with the electromagnetic near-field generated at the inner hot-spots are responsible for the chiroptical response.

Relevant factors for the optical activity of chiral plasmonic nanostructures are the nanoparticle size, the nature of the nanoparticle and the molecule, and the molecule–NP distance. The Coulomb dipole–dipole interaction dominates the coupling between the molecule and NP when the distance is small and the CD signal of the system results from the sum of the CD of the molecule and the CD of the plasmon.[74]

Potential applications of these chiral nanomaterials are: chiral sensing, biorecognition and chiroptic. In addition, chiral AuNPs are particularly promising for asymmetry amplification, such as in enantioselective chemical synthesis. Chiral AuNPs could enable detection of weak induced circular dichroism of chromophores and be used for specific recognition of chiral biological molecules, as required for therapeutic applications. Moreover, these nanoparticles can be used as chiral dopants in liquid crystals,[75] e.g., AuNCs functionalized with axially chiral binaphthyls have been exploited as additives in achiral liquid crystal phases to generate chiral nematic liquid crystal phases.[49] The use of chiral AuNPs in LC allows to control the size, shape and self-assembly of NPs in one-pot process which is essential to integrate them into high-tech devices such as light scattering devices or flat panels.[2,76] Furthermore, these LC-containing organized AuNPs have potential applications as electrical actuators, sensors or more efficient photocatalysts.[77]

In addition, chiral gold nanorods (AuNRs) deposited on a TiO_2 surface have revealed that the handedness of the nanomaterial can be reversed via a photo-induced process; the chirality switch, achieved by irradiating either with left or right-CPL, was maintained even in the absence of external stimuli.[78] Therefore, chirality can be imprinted in achiral metallic nanoparticles for tuning electrical and optical properties that may be suitable for fabricating optoelectronics and in bio-applications. In terms of their potential application in disease treatment, in particular Alzheimer's disease, Tang and co-workers[79] synthesized *L*- and *D*-GSH-capped AuNPs, that permeate the blood–brain-barrier through several GSH channels in the human brain, to preclude the aggression of the beta-amyloid 42 (Aβ42), resulting in a disease treatment.

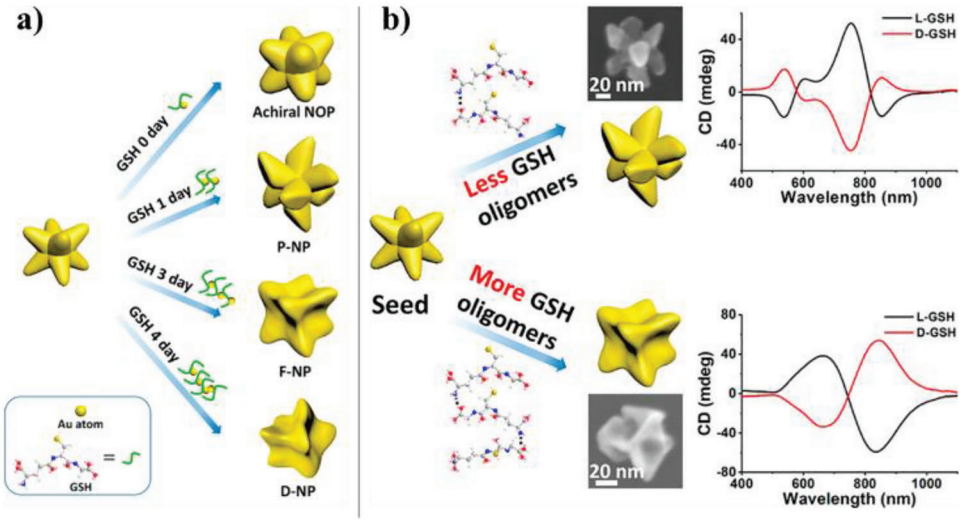

Figure 10. a) Scheme of the synthesis of different-morphology AuNPs prepared with *L*-GSH and at incubation times of 0, 1, 3, and 4 days. b) Propeller- and flower-like chiral AuNPs obtained from Au nano-octopods by modulation of its chiral morphology adding *L*-glutathione (GSH) with a different incubation time degree of oligomerization. Left: Comparison of the CD spectra of the AuNPs prepared by using *L*-or *D*-GSH as the modulator agent. Reproduced with permission.[73] Copyright 2021, American Chemical Society.

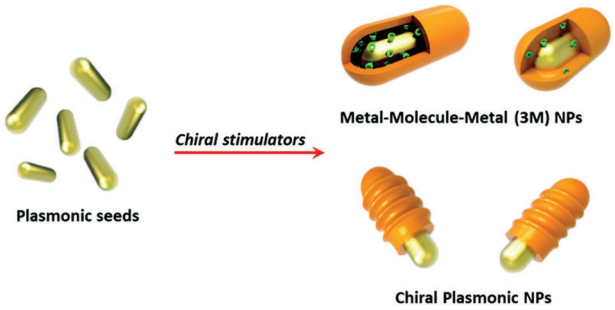

Figure 11. Schematic representation of the two main strategies for the synthesis of chiral plasmonic NPs from pre-synthesized plasmonic seeds. Reproduced with permission.[74] Copyright 2021, Royal Society of Chemistry.

5. Chiroptical Response in Upconversion Nanoparticles

UCNPs consist of a lanthanide-doped matrix, e.g., $NaYF_4$:Yb,Tm. They are a class of photoactive nanomaterials that can convert low-energy photons (near-infrared, NIR, photons) into high energy photons (UV–vis) at a more efficient rate than other materials. As a consequence, they emit in the UV, VIS and even in the NIR, process known as upconversion luminescence (UCL).[80] UCNPs display exceptional optical properties, such as multiple and narrow emission bands, non-photobleaching, non-photoblinking, long luminescence lifetimes, high stability and low cytotoxicity.[81–83] Especially, the use of NIR excitation light has attracted the attention of researchers during the last decade due to its high penetration depth in tissues, as well as low background autofluorescence in biosamples.[84]

Hence, UCNPs have been used for different widespread applications such as in bioimaging, phototherapy or biosensing, but also in anticounterfeiting, solar cells, or photocatalysis.[85–91]

It should be noted that UCNPs are achiral materials, however, the construction of nanoassemblies between two kinds of nanoparticles can endorse the UCNP-containing nanoplatform with chiroptical properties, since minor changes in the geometry of the assemblies can strongly modify the CD optical properties of the nanohybrids.[92,93] In this way, Wu et al. built a tetramer in solution composed of one Yb/Er co-doped $NaGdF_4$ UCNPs surrounded by three AuNRs, **Figure 12**a).[94] The nanoassembly between both nanoparticles was reached through the DNA hybridization between complementary strands attached conveniently to both nanoparticles. The resulting tetramers displayed strong chiroptical activity, while the individual nanoparticles response was weak (Figure 12b). The tetramers displayed different CD bands which were tuned by modifying the length of the DNA sequence, the plasmonic properties of the AuNRs and UCNP size. Thus, the largest g-factor was found for a DNA strand of 11 base pairs, AuNRs with a plasmon at 750 nm and 20 nm-sized UCNPs. The authors demonstrated that the chiroptical activity of the AuNR-UCNP tetramers was due to their propeller-like geometry.

In addition to the chiral optical activity, the UCL was enhanced due to the plasmonic coupling and also the enhancement degree was dependent on the distance between both nanoparticles, reaching the maximum at 30 nm.[95] Furthermore, the nanoassembly was successfully applied for the detection in solution of a cancer biomarker, specifically hepatitis A virus Vall7 polyprotein gene (HVA), by designing a convenient homogeneous assay Figure 12c–f. Upon recognition of the target, the distance between both nanoparticles was enlarged and consequently, both CD and UCL signal decreased when using increasing concentrations of the target (Figure 12c,e, respectively). The limit of detection (LOD) calculated from the calibration curves was as low as 13.2 and 20.3 aM for the CD and UCL-based assays, respectively. This study represents a major step forward in the engineering of structures for biosensing combining

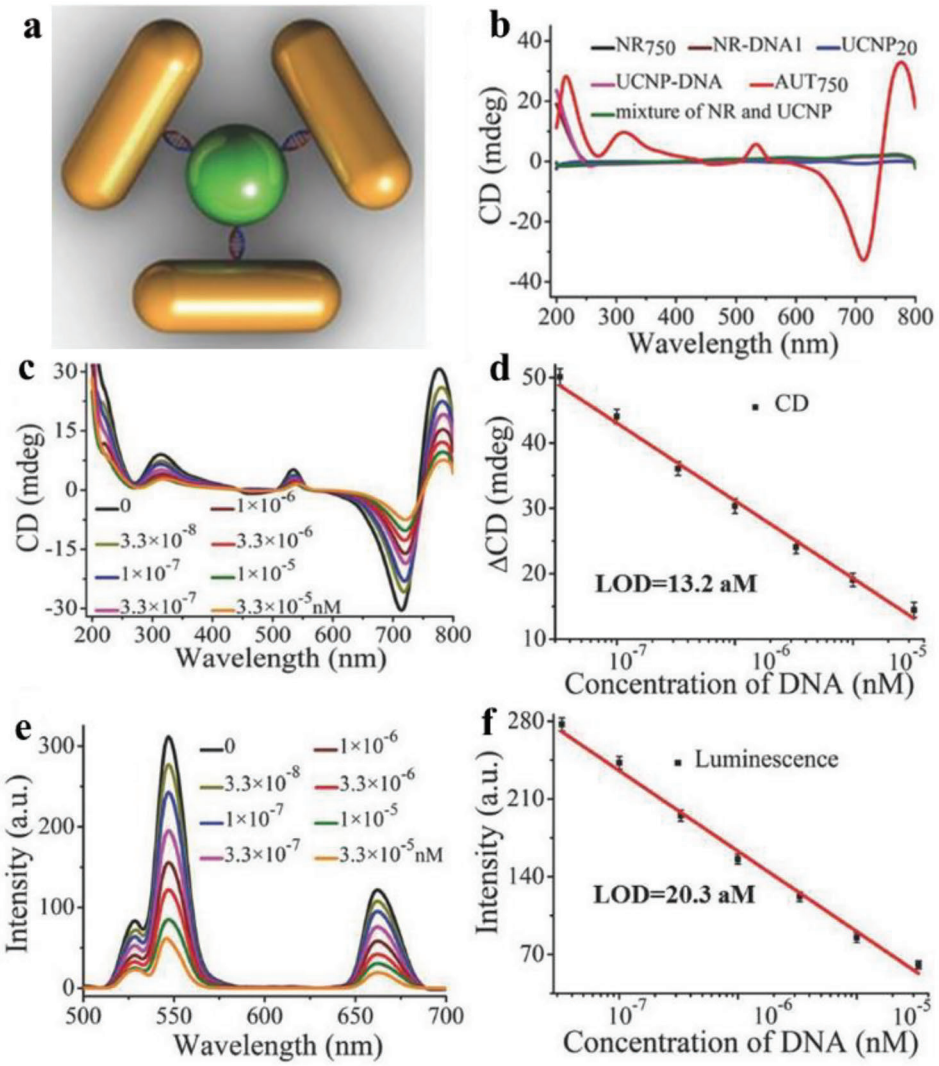

Figure 12. a) Geometric structure illustrations of the top view of the tetramer. b) Experimental CD of the NR-UCNP tetramer assemblies (red line) in comparison to their controls: unfunctionalized NR (black), DNA-modified NR (brown), unfunctionalized UCNPs (blue), DNA-functionalized UCNPs (pink) and a mixture of NR and UCNPs (green). c–f) DNA detection with the NR-UCNP tetramer assembly. c) CD and e) UC luminescence spectra with increasing concentrations of DNA in the solution. Calibration curves with the estimated LOD for DNA detection by d) CD and f) UCL. Adapted and reproduced with permission.[94] Copyright 2016, WILEY-VCH Verlag GmbH & Co.

chiroptical and luminescent activity for the improvement of the reliability and versatility of the detection.

Similarly, the same group designed a pyramid nanoassembly consisting of two $NaGdF_4$:Yb^{3+},Er^{3+} UCNPs and two spherical AuNPs for the intracellular detection of micro-RNA (miRNA).[96] For the formation of the pyramids, two homogenous AuNPs and UCNPs dimers were synthesized first via hybridization of the DNA strands on the surface of both NPs. Then, the pyramid was assembled by hybridization of two dimers. The assembled pyramid displayed chiroptical activity in the visible region where the intracellular substances do not have a chiroptical response (biomolecules are optically active in the UV region). In this case, the UCL was quenched in the pyramids by resonant energy transfer from the UCNPs to the AuNPs. The pyramids were ingeniously designed to provoke the separation of the UCNPs and AuNPs upon recognition of the miRNA21 target. Therefore, the UCL signal of the UCNPs was restored and the CD activity of the pyramids disappeared. Moreover, the nanoassembly was successfully applied for dual-mode ultrasensitive detection of miRNA21 in living HeLa cells. The LOD of the CD signal was 0.03 fmol/10 μg_{RNA} and 0.12 fmol/10 μg_{RNA} for the UCL signal.

Moreover, the use of porous materials like metal–organic framework (MOF) proved to be useful to integrate within one system UCNPs and a chiral component. As an illustrating example, core $NaYF_4$:Yb^{3+},Er^{3+} UCNPs were covered with a layer of zeolitic imidazolate framework-8 (ZIF-8) MOF decorated with chiral NiS_x NPs.[97] The chirality of the UCNPs containing nanoassembly was confirmed by the presence of two intense CD signals at 440 and 530 nm, which were similar to those from the NiS_x NPs. Moreover, the CD signals decreased with increasing concentrations of H_2O_2 due to the degradation of the NiS_x in presence of H_2O_2, taking place the conversion of UCNP@ZIF-NiS_x into

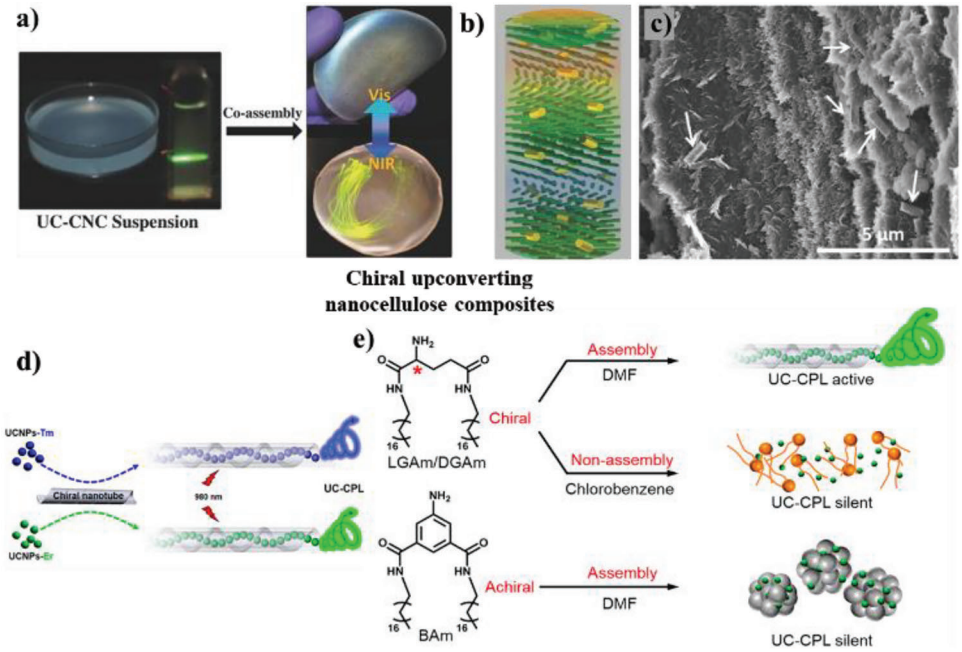

Figure 13. a) Representation of the procedure for the co-assembly of lyotropic cellulose liquid crystals with PVA-stabilized $NaYF_4$:Yb^{3+},Er^{3+} hexagonal nanorods into nanostructured cellulose films. b) Schematic of chiral nematic structure in the composites. c) SEM images of the composite films. Adapted with permission.[98] Copyright 2016, Wiley-VCH. d) Schematic representation of UC-CPL induced in achiral UCNPs through their assembly into chiral nanotubes. e) Possible explanation for the presence and absence of UC-CPL in the different synthesis carried out in the work. Adapted with permission.[99] Copyright 2019, American Chemical Society.

UCNP@ZIF. Under physiological conditions, the sensor worked in an H_2O_2 concentration range of 0.05 to 20 μM and the LOD was 0.032 μM. Notably, due to the biocompatibility of the components, the nanoassembly was successfully implemented as ROS sensor in living normal primary uterine fibroblast cells (PCS-460-010) as well as in vivo by using a tumor-bearing mouse model.

Another strategy to create an UCNP-based nanostructure with chiroptical activity is the use of a chiral host matrix. Nguyen et al., combined cellulose nanocrystals (CNC) as a chiroptical nematic host matrix and polyvinylalcohol (PVA)-stabilized $NaYF_4$:Yb^{3+},Er^{3+} UCNPs as a photoactive guest in a helicoidal nanocomposite (**Figure 13**a–c).[98] A strong positive band at ≈500 nm was observed in the CD spectrum of the UCNP-CNC nanocomposites indicating that the reflection of LCP was preferred, and consequently, that the chiral nematic organization of CNCs was maintained in the nanocomposite.

To date, few UCNPs with induced UC-CPL properties have been described. They have been applied for different purposes, e.g. to trigger the enantioselective photopolymerization of diacetylene (DA) derivatives.[99] In this work, chiral nanotubes were formed during the gelation of a chiral lipid gelator, in particular *N*,*N*-bis(octadecyl)-*L*-glutamic diamide (*L*-GAm) and its enantiomer *D*-GAm.[100] Moreover, achiral UCNPs, such as $NaYF_4$:Yb^{3+},$Er^{3+}$and $NaYF_4$:Yb^{3+},Tm^{3+} nanoparticles were helically encapsulated into these chiral nanotubes during the gelation process (Figure 13d). When the UCNPs were co-assembled with *L*-GAm/*D*-GAm, the system displayed the mirror-image UC-CPL signals upon excitation with nonpolarized 980 nm light. However, no UC-CPL signal was detected in co-assemblies with 2,6-dichlorbenzamid (Bam, achiral analog molecule to *L*-GAm/*D*-GAm) or in unassembled chiral gelator/UCNPs mixtures. These facts evidenced that the mechanism for UC-CPL was "chiral host-UCNP guest" and, consequently, the well-ordered arrangement of UCNPs in a chiral manner is critical to induce a chiroptical response of the assembly; moreover, the chirality transfer from the *L*-GAm and *D*-GAm monomers to UCNPs was not possible (Figure 13e).

Interestingly, the UC-CPL, generated at the UV region from Tm-doped UCNP co-gels, triggered the photopolymerization of 2,4-heneicosadiynoic acid (HA) to polydiacetylene (PDA) in a film. Most importantly, the resulting photopolymerization product exhibited CD signals which were positive or negative when irradiated *L*-GAm/UCNPs-Tm and *D*-GAm/UCNPs-Tm co-gels, respectively. These results clearly evidenced that the molecular chirality of the gelator (*L*-GAm or *D*-GAm) directed the handedness of the UC-CPL generated from the respective co-gels and, therefore, the co-gels were able to undergo the polymerization of PDA enantioselectively.

Similarly, the asymmetric photopolymerization of PDA from 10,12-pentacosadiynoic acid (PA) was achieved through excitation with NIR light of a nanohybrid consisting of $NaYF_4$:Yb^{3+},Tm^{3+}@$NaYF_4$ UCNPs and cysteine-modified AgNPs as the chiral source.[101] This work demonstrated that the screw direction of the resulting helical PDA chains upon NIR irradiation of a film containing PA and the UCNP-AgNP@cys nanohybrids was dictated by the AgNP@cys, i.e., the PDA chains were predominantly left-handed (evidenced by the negative Cotton effect in CD spectrum) when AgNP@L-cys were used and

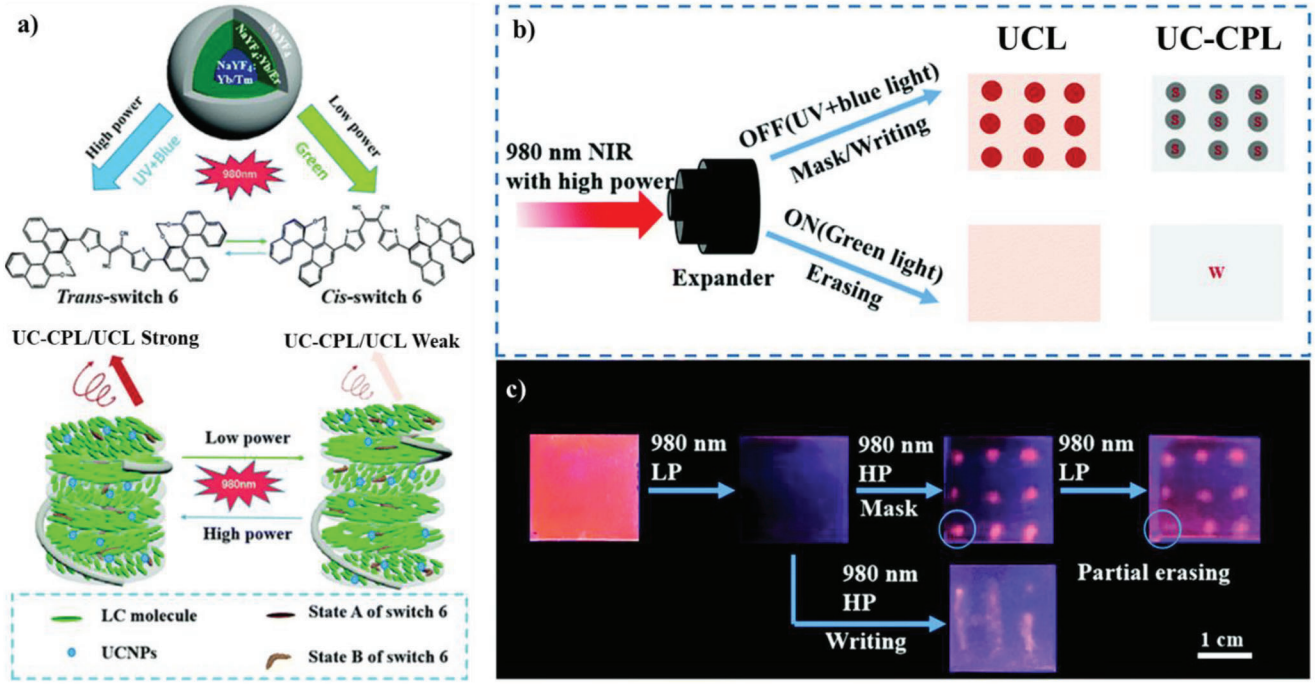

Figure 14. a) Schematic illustration of the photoisomerization of switch 6 upon excitation at 980 nm and the reversible tuning of the helical superstructures containing UCNPs upon NIR irradiation at different power densities. b) Diagram of the illumination of the UCL and UC-CPL rewritable optical storage. c) Real images of UCL/UC-CPL dual-mode patterns. Adapted with permission.[102] Copyright 2020, Royal Society of Chemistry.

strong positive CD signals were observed when AgNP@*D*-Cys were employed due to the preferential formation of right-handed PDA helix.

In addition, the handedness of the CPL induced in UCNP-based nanohybrids can be reversibly switched by modulating the power intensity of the NIR light.[102] As an example, cholesteric liquid crystal (CLC) with a self-organized helical superstructure was employed as the matrix for loading β-$NaYF_4$:Tm^{3+},Yb^{3+}@$NaYF_4$:Er^{3+},Yb^{3+}@$NaYF_4$ core/shell/shell UCNPs and a chiral fluorescent switch, namely a derivative of the (*R*)-1,1'-binaphthol (**Figure 14**a). The *trans*-to-*cis* photoisomerization of the fluorescent switch was effectively triggered by 520 nm green light, and the reverse photoisomerization took place upon irradiation at 365 or 450 nm light. Curiously, the designed core/shell/shell UCNPs exhibited a UCL emission where: i) the intensity of the green emission band (≈520 nm) is the highest at a low-power density NIR excitation (0.15 W mm^{-2}) and ii) the intensity of the UV bands (350–470 nm region) was greatly enhanced at a high-power density of the NIR light (3.0 W mm^{-2}). This observation evidenced the UCL mechanism can be controlled with the power density of the excitation source;[103] at low energy excitation, the $Yb^{3+}\rightarrow Er^{3+}$ energy transfer mechanism dominated while at high-power density excitation governed the $Yb^{3+}\rightarrow Tm^{3+}$ energy transfer mechanism. Most importantly, the Er^{3+} emission at 520 nm overlapped with the absorption spectrum of the *trans* form of the fluorescent switch, while the Tm^{3+} emission overlapped with the absorption of the *cis* form. Consequently, upon irradiation at a low power density of the fabricated CLC material, the UCL emission at 520 nm was favored and triggered the photoisomerization of the fluorescent switch from *trans* to *cis*, yielding a strong decrease of both the UCL and CPL intensity of the CLC system.[102] This process can be reverted by increasing the excitation power density. As demonstrated by the authors, this helical superstructure has potential application in the construction of NIR-activated, optically-rewritable UCL patterns as well as of CPL patterns (Figure 14b,c).

Recently, it has been described that the spin-coating of Tm/Nd co-doped UCNPs on a gold plasmonic chiral metasurface endowed the nanohybrid with UC-CPL properties.[104] This nanomaterial exhibited a strong and modulable UC-CPL from Tm^{3+} and Nd^{3+} emitters triggered by the resonant coupling between surface plasmons and UCNPs.

Chiral helical materials are widely employed as the matrix for building nanoparticle-based nanohybrids with chiroptical activity. However, it is worth noting that not necessarily the self-organized helical material must be chiral or contain a chiral element. As demonstrated by Zhou et al. a nanohybrid displaying UC-CPL optical property can be achieved by using only achiral counterparts.[105] The co-assembly of the achiral molecule, C3-symmetric benzene-1,3,5-tricarboxamid (BTABA), and UCNPs led to a supramolecular nanohelix with induced chirality and UC-CPL behaviors, which can be attributed to the supramolecular chirality of the system. The chirality transfer in the helical BTABA-UCNPs co-assembly was produced via a noncovalent interaction in a similar way to that found for the *L*- and *D*- Cys to UCNPs described above. Furthermore, the UC-CPL peaks can be easily tuneable by changing the type of lanthanide cations in the UCNP architecture, i.e., in the range between 425 to 500 nm for Yb/Tm co-doped UCNPs or two UC-CPL peaks at 538 and 653 nm for Yb/Er co-doped UCNPs.

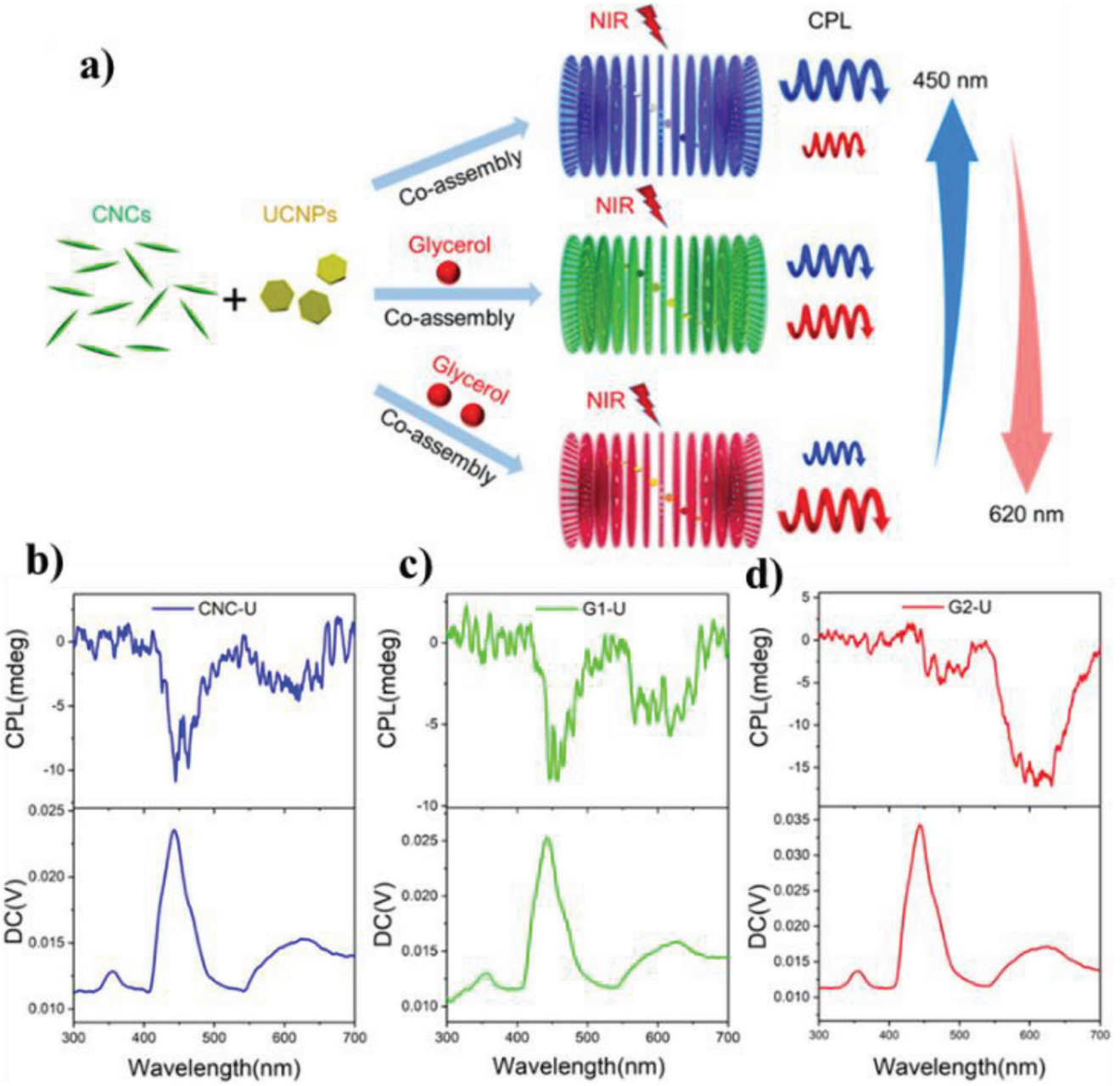

Figure 15. a) Illustration showing the tunability of the UC-CPL emission from the chiral photonic films with the glycerol content. b–d) UC-CPL and CD spectra of the nanomaterials with different amounts of glycerol: b) No glycerol, c) 0.02 g of glycerol, and d) 0.04 g of glycerol. Adapted with permission.[106] Copyright 2019, American Chemical Society.

Besides that, tuneable UC-CPL can be also achieved by precisely tuning the chiroptical properties of the host.[106] Right-handed UC-CPL (negative signals) was observed in films containing $NaYF_4$:Yb^{3+},Tm^{3+} and CNC-based chiral photonic hosts whose peak maximum was red-shifted with increasing amounts of glycerol in the sample. Glycerol acted as an external stimulus to modify the photonic bandgaps of the CNC-based photonic films (**Figure 15**a). Considering that only photons with a particular wavelength can pass through the film, i.e., photon propagation is forbidden when the emission occurs inside the photonic band gap (PBG), while spontaneous emission can take place from photons outside PBG, and the multiple UC-CPL bands of the film upon NIR excitation, the selective chiral amplification of the photonics bandgaps with the content of glycerol allowed the modification of the UC-CPL peak maxima of the film. Specifically, the forbidden nature of UCL at 450 nm (overlapping with PBG) led to greater g_{lum} values, while the UCL emission at 620 nm (far from its PBG) originated smaller g_{lum} values.

Thus, three different films were fabricated with increasing amounts of glycerol showing a red-shifted UC-CPL peak maxima (Figure 15b–d). Apart from UC-CPL chiroptical activity, these photonics films were able to reflect CPL displaying also different iridescent colors.

Furthermore, strategies to improve UC-CPL in nanomaterials have been recently explored.[107,108] The first example of UC-CPL enhancement was reported in a material that integrated $NaYF_4$:Yb^{3+},Tm^{3+} UCNPs and $CsPbBr_3$ lead halide perovskite nanocrystals (HP NCs) into a chiral NLC composed by the achiral nematic liquid crystal SLC1717 and chiral dopant *R*(*S*)811.[107] The photonic bandgaps of the NLC was tuned by adjusting the weight ratio of *R*811/*S*LC1717 in order to locate the emission of the $CsPbBr_3$ HP NCs and UCNPs in the centre and left side, respectively, of the photonics bandgaps for obtaining UC-CPL.[109] Due to the transfer of chirality from the NLC to the nanoparticles, UC-CPL peaks from both UCNPs (at 475 nm) and HP NCs (at 495 nm) were detected, the latter caused by resonance energy transfer (RET) from the UCNP to HP NCs upon 980 nm excitation. The PBG adjustment enabled an enhancement of both UC-CPL intensity with a $\geq_{lum}$ value of 0.4 and 1.1 for the UC-CPL of UCNPs and HP NCs, respectively. To our knowledge 1.1 is the largest $\geq_{lum}$ reached for UC-CPL. This strategy has been studied previously in some molecular co-assembled systems[20,110–113] and is known as energy transfer amplified circular polarization, where the energy transfer process can be considered as circularly polarized excitation that amplifies the CPL signals.

Following this premise, more recently, Yb/Tm UCNPs were embedded into a chiral structure of $CsPbX_3$ HP NCs.[108] The chirality in HP NCs arose from ligand chirality due to their functionalization with (*R*)/(*S*)-2-aminooctane. The chiroptical activity of the UCNPs induced by their confinement into a chiral space, i.e., chiral HP NCs, was further corroborated by UC-CPL spectra after the excitation of the nanomaterial at 980 nm. As in the previous example, the HP NCs can also emit CPL upon NIR excitation due to the energy transfer process from UCNPs. In this case, the $\geq_{lum}$ value was 4.5×10^{-3} which was four times higher than the observed in the CPL of analogous chiral HP NCs ($\geq_{lum}$ = 1.1×10^{-3}) excited at 400 nm. The authors attributed this enhancement to the energy transfer process from UCNPs to HP NCs which included the resonance helicity transfer and chiral photon reabsorption between UCNP and LHP.

6. Conclusions

To sum up, nanotechnology is rapidly progressing to create artificial chiral nanomaterials. The origin of the nanoparticle chirality (summarized in **Table 1**) can vary with its nature or be similar for nanomaterials of different composition and can include: the natural occurrence of chiral defects, intrinsic chirality of crystal lattice (e.g., in semiconductor nanocrystals), such as screw dislocation that propagates through the crystal, and chiral morphology (in metal and semi-conductor nanoparticles), or by placing the achiral nanoparticle in a chiral environment, the use of chiral ligands molecules during the synthesis, as well as by using of mixture of chiral/achiral ligands. Analogously, the encapsulation of achiral nanoparticles in chiral matrix such as a chiral lipid gelator or nematic liquid crystals, can endow the final nanomaterial with chiroptical activity thanks to the "chiral host-achiral guest" interaction. In addition, the formation of geometrical nanoassemblies such as pyramids o tetrapods comprising more than one nanoparticle, whether they are of the same or different chemical nature, can endow the final nanoassembly with optical chirality response. It should be noted that the chiral activity of the nanoassembly is higher for nanoassemblies with chiral frames such as helical geometry.[114]

Either by intrinsic or induced chiroptical activity, chiral up- and down- shifting inorganic nanoparticles have triggered numerous applications in various fields, such as sensing, optoelectronics, enantioselective photocatalysis, photopolymerization or even disease treatment. For example, CD response depends on structure and composition of plasmonic NPs, such as AuNPs. Further optimization of NPs is needed to generate a chiral field, which enhances the chirality and could be used for highly sensitive detection of biomolecules, such as glucose or DNA. In addition, ultrafast pump-probe technology could provide time-resolved CD spectrum and give dynamic information of molecule structures.

With respect to chiral metal clusters, they provide atomically precise structure information and their biocompatibility can enable their application in sensing of chiral bioactive compounds. However, the detection sensitivity and selectivity need to be still improved. Despite that, they can have a tremendous potential for asymmetric catalysis, but there are still few relevant examples.

Regarding chiral perovskites, the reported studies have mostly focused on lead-based chiral perovskites. However, the toxicity of lead and the relative low stability of these materials to ambient conditions are important challenges that should be overcome for their potential applications. Chiral lead-free hybrid double perovskites based on the assembling of chiral organic cation with Ag^+ and Bi^{3+} have shown intrinsic chirality resulting from the transfer of chirality from organic cations to the perovskite framework.[115] Thus, CD measurements of $[(R)\text{-}\beta\text{-MPA}]_4AgBiI_8$ ((R)-β-MPA = (R)-(+)-β-methylphenethylammonium) of this perovskite exhibit notable chirality induced by organic cations (the self-powered circularly polarized light anisotropy factor up to 0.3; the highest value among reported chiral perovskites).

The intriguing optical properties of UCNPs, i.e., UV/Vis/NIR emission upon NIR excitation, make them very attractive for emerging optical and biological applications, especially for sensing purposes. Different strategies have been envisaged to endorse naturally achiral UCNPs with chirality, e.g., ligand chirality transfer or the use of chiral host matrix. Nevertheless, the main handicap is their low UCL quantum yield as well as low g_{lum} factor values obtained which may hinder their further development. Hence, more sophisticated designs based on plasmonic-enhancement[104] or energy transfer between different types of nanoparticles are required to improve efficiently the chiroptical activity of these nanomaterials. Specifically, energy transfer amplified circular polarization greatly enhanced the g_{lum} factor in UCNPs-based systems allowing the highest value (1.1) for a nanohybrid with UC-CPL response.

Despite the significant advance in the field of chiral nanoparticles, it still needs more investigation in the future from the fundamental understanding of the origin of the chiral activity to their further applications. The rational design and optimization of nanostructures containing inorganic nanoparticles will be essential for the successful development and implementation of these chiral nanomaterials into real-life applications.

Table 1. Summary of the chiroptical active nanomaterials characteristics introduced in this review.

Material	g_{abs}	g_{lum}	Enantiomeric excess	Chirality origin	Ligand	Ref.
CdTe	$2\text{-}4\times10^{-5}$	–	30%	Circularly polarized light induced	TGA	[13]
TNCs	$1\text{-}6\times10^{-4}$	–	–	Ligand induced	PVP-*D*/*L*-cys	[15]
$Au_{20}(PP_3)_4Cl_4$	3.46×10^{-3}	–	97%	Electron transitions confined in the Au core	tris(2-(diphenylphosphino)ethyl) phosphine (PP_3)	[31]
AgNCs	–	–	–	Ligand induced	DNA	[32]
Au_4NCs	–	–	–	Ligand induced	*N*-acetyl-l-cysteine	[36]
AuNCs	1×10^{-4}-1×10^{-3}	–	—	Ligand induced	PET	[37]
$[Au_{13}(dppe)_5Cl_2]\ Cl_3$	$1\text{-}5\times10^{-3}$	–	–	Ligand induced	dppe	[38]
AuNCs	6×10^{-4}	–	–	Ligand induced	DIOP-Xantphos	[39]
AuNCs	1.6×10^{-3}	–	Enantiopure	Ligand induced	dppe	[41]
AuNCs	10^{-3}	–	Enantiopure	Intrinsic	PET	[43]
AuNCs	5×10^{-4}	–	80%	Ligand induced	*N*-isobutyryl-d-cysteine	[45]
AuNCs	–	–	–	Chiral inversion	Penicillamine	[47]
AuNCs	–	–	–	Ligand induced	TBA	[48]
$CsPb(I/Br)_3$	1.5×10^{-3}	–	Enantiopure	Ligand induced, surface distortion, electronic interactions	DACH	[56]
$CsPbBr_3$	2.4×10^{-4}	7×10^{-3}	Enantiopure	Ligand induced	α-octylamine	[57]
$(MBA)_2PbI_{4(0.7)}\ Br_{4(0.3)}$	1×10^{-3}	–	–	Ligand induced	MBA	[59]
$MPEAPbBr_3$	6.5×10^{-3}	–	–	Intrinsic	MPEA	[60]
$CYHEAPbI_3$	–	–	Enantiopure	Ligand induced	1-cyclohexylethylamine (CYHEA)	[61]
$(MBA)_2PbI_4$	–	–	Enantiopure	Ligand induced	MBA	[62]
AgNPs	–	–	Enantiopure	Ligand induced	Glutathione	[67]
AuNPs	–	–	–	Intrinsic	Hexadecyltrimethylammonium bromide	[68]
AuNPs	0.2	–	–	Ligand induced	Cysteine and glutathione	[70]
AuNPs	0.02	–	–	Formation chiral shapes directed by ligand	g-Glu-Cys and Cys-Gly	[71]
AuNPs	0.02	–	–	Ligand induced	Cys	[72]
AuNPs	$2\text{-}3\times10^{-3}$	–	Enantiopure	Formation chiral shapes directed by ligand	Glutathione	[73]
AuNPs	–	–	43-70%	Intrinsic and photoinduced	Hexadecyltrimethylammonium bromide	[78]
AuNPs	–	–	–	Ligand induced	Glutathione	[79]
UCNPs-AuNPs	0.02	–	–	Chiral geometry nanoassembly	DNA	[94]
UCNPs-AuNPs	–	–	–	Chiral geometry nanoassembly	DNA	[96]
UCNP@ZIF-NiSx	–	–	Enantiopure	NP induced (from chiral NiSx NPs)	Chiral penicillamine template	[97]
UCNPs	–	–	Enantiopure	Chiroptical host matrix (CNC)	PVA	[98]
UCNPs	–	5.5×10^{-3}	Enantiopure	Chiroptical host matrix (Glutamic diamide)	Oleic acid	[99]
UCNPs-AgNPs	–	0.04	Enantiopure	NP induced (from chiral AgNPs)	Cys	[101]
UCNPs	–	0.49	–	Chiroptical host matrix	Oleic acid	[102]
UCNPs	–	0.95	–	Plasmonic chiral metasurface	Oleic acid	[104]
UCNPs	–	0.012	–	Chiroptical host matrix (BTABA)	11-aminoundecanoic acid	[105]
UCNPs	–	0.033-0.156	–	Chiral host matrix (CNC)	PVA	[106]
UCNPs-$CsPbBr_3$	–	1.1	–	Chiral host matrix (NLC)	Oleic acid	[107]
UCNPs-$CsPbBr_3$	–	1.1×10^{-3}	99%	NP induced (from chiral LHPNCs)	α-aminooctane and oleic acid	[108]
CdSe/ZnS	–	1.8	–	Chiral host matrix (cholesteric glass-forming matrix)	Trioctylphosphine oxide	[109]

Acknowledgements

The authors thank the Spanish Ministry of Science and Innovation (MCIN), projects PID2020115710GB-I00, Agencia Estatal de Investigación-AEI and MICIU Unit of Excellence "Maria de Maeztu" CEX2019-000919-M, as well as the Generalitat Valenciana projects PROMETEO/2019/80 and IDIFEDER/2018/064, all of them partially co-financed with FEDER funds. L.F.S. thanks the Spanish Ministry of Universities for her Maria Zambrano contract (ZA21-037, financed by the European Union, NextGeneration EU).

Conflict of Interest

The authors declare no conflict of interest.

Keywords

chiroptic, gold nanocluster and nanoparticles, lanthanide-doped nanoparticles, lead halide perovskite, upconversion nanoparticles

Received: February 10, 2023
Revised: April 25, 2023
Published online:

[1] L. Zhang, H.-X. Wang, S. Li, M. Liu, *Chem. Soc. Rev.* **2020**, *49*, 9095.
[2] X. Zhang, Y. Xu, C. Valenzuela, X. Zhang, L. Wang, W. Feng, Q. Li, *Light Sci Appl* **2022**, *11*, 223.
[3] R. W. Woody, *Methods Enzymol.* **1995**, *246*, 34.
[4] N. S. S. Nizar, M. Sujith, K. Swathi, C. Sissa, A. Painelli, K. G. Thomas, *Chem. Soc. Rev.* **2021**, *50*, 11208.
[5] M. Wakabayashi, S. Yokojima, T. Fukaminato, K. Shiino, M. Irie, S. Nakamura, *J. Phys. Chem. A* **2014**, *118*, 5046.
[6] T. Zhao, J. Han, P. Duan, M. Liu, *Acc. Chem. Res.* **2020**, *53*, 1279.
[7] J. P. Riehl, F. S. Richardson, *Chem. Rev.* **1986**, *86*, 1.
[8] J. J. Pelayo, I. Valencia, A. P. García, L. Chang, M. López, D. Toffoli, M. Stener, A. Fortunelli, I. L. Garzón, *Adv. Phys. X* **2018**, *3*, 1509727.
[9] J. Liu, L. Chen, H. Cui, J. Zhang, L. Zhang, C.-Y. Su, *Chem. Soc. Rev.* **2014**, *43*, 6011.
[10] J. K. Gansel, M. Thiel, M. S. Rill, M. Decker, K. Bade, V. Saile, G. von Freymann, S. Linden, M. Wegener, *Science* **2009**, *325*, 1513.
[11] N. H. Cho, A. Guerrero-Martínez, J. Ma, S. Bals, N. A. Kotov, L. M. Liz-Marzán, K. T. Nam, *Nat. Rev. Bioeng.* **2023**, *1*, 88.
[12] Y. Shao, G. Yang, J. Lin, X. Fan, Y. Guo, W. Zhu, Y. Cai, H. Huang, D. Hu, W. Pang, Y. Liu, Y. Li, J. Cheng, X. Xu, *Theranostics* **2021**, *11*, 9262.
[13] J. Yeom, B. Yeom, H. Chan, K. W. Smith, S. Dominguez-Medina, J. H. Bahng, G. Zhao, W.-S. Chang, S.-J. Chang, A. Chuvilin, D. Melnikau, A. L. Rogach, P. Zhang, S. Link, P. Král, N. A. Kotov, *Nat. Mater.* **2015**, *14*, 66.
[14] N. Gaponik, D. V Talapin, A. L. Rogach, K. Hoppe, E. V Shevchenko, A. Kornowski, A. Eychmüller, H. Weller, *J. Phys. Chem. B* **2002**, *106*, 7177.
[15] X. Li, P. Chen, Y. Xia, J. Weng, M. Chen, T. He, Y. Li, J. Cheng, L. Zhang, *J. Phys. Chem. Lett.* **2022**, *13*, 11669.
[16] W. Feng, J.-Y. Kim, X. Wang, H. A. Calcaterra, Z. Qu, L. Meshi, N. A. Kotov, *Sci. Adv.* **2023**, *3*, e1601159.
[17] M. Song, L. Tong, S. Liu, Y. Zhang, J. Dong, Y. Ji, Y. Guo, X. Wu, X. Zhang, R.-Y. Wang, *ACS Nano* **2021**, *15*, 5715.
[18] J. Lv, X. Gao, B. Han, Y. Zhu, K. Hou, Z. Tang, *Nat. Rev. Chem.* **2022**, *6*, 125.
[19] W. Ma, L. Xu, A. F. de Moura, X. Wu, H. Kuang, C. Xu, N. A. Kotov, *Chem. Rev.* **2017**, *117*, 8041.
[20] Y. Sang, J. Han, T. Zhao, P. Duan, M. Liu, *Adv. Mater.* **2020**, *32*, 1900110.
[21] S. M. van de Looij, E. R. Hebels, M. Viola, M. Hembury, S. Oliveira, T. Vermonden, *Bioconjug Chem* **2022**, *33*, 4.
[22] R. Jin, C. Zeng, M. Zhou, Y. Chen, *Chem. Rev.* **2016**, *116*, 10346.
[23] L. Haye, P. I. Diriwari, A. Alhalabi, T. Gallavardin, A. Combes, A. S. Klymchenko, N. Hildebrandt, X. Le Guével, A. Reisch, *Adv. Opt. Mater.* **2022**, 2201474.
[24] A. Bonanno, I. Pérez-Herráez, E. Zaballos-García, J. Pérez-Prieto, *Chem. Commun.* **2020**, *56*, 587.
[25] D. Cuaran-Acosta, P. Londoño-Larrea, E. Zaballos-García, J. Pérez-Prieto, *Chem. Commun.* **2019**, *55*, 1604.
[26] Y. Shichibu, Y. Negishi, H. Tsunoyama, M. Kanehara, T. Teranishi, T. Tsukuda, *Small* **2007**, *3*, 835.
[27] I. Pérez-Herráez, M. Justo-Tirado, M. Bueno-Cuenca, E. Zaballos-García, J. Pérez-Prieto, *Nanoscale Adv* **2022**, *4*, 2250.
[28] Y. Zhu, J. Guo, X. Qiu, S. Zhao, Z. Tang, *Accounts Mater. Res.* **2021**, *2*, 21.
[29] A. Guerrero-Martínez, J. L. Alonso-Gómez, B. Auguié, M. M. Cid, L. M. Liz-Marzán, *Nano Today* **2011**, *6*, 381.
[30] C. Noguez, I. L. Garzón, *Chem. Soc. Rev.* **2009**, *38*, 757.
[31] Y. Zhu, H. Wang, K. Wan, J. Guo, C. He, Y. Yu, L. Zhao, Y. Zhang, J. Lv, L. Shi, R. Jin, X. Zhang, X. Shi, Z. Tang, *Angew. Chem., Int. Ed.* **2018**, *57*, 9059.
[32] J. T. Petty, J. Zheng, N. V. Hud, R. M. Dickson, *J. Am. Chem. Soc.* **2004**, *126*, 5207.
[33] T. L. Wetzel, A. E. DePristo, *J. Chem. Phys.* **1996**, *105*, 572.
[34] G. Shemer, O. Krichevski, G. Markovich, T. Molotsky, I. Lubitz, A. B. Kotlyar, *J. Am. Chem. Soc.* **2006**, *128*, 11006.
[35] C. L. Cleveland, U. Landman, T. G. Schaaff, M. N. Shafigullin, P. W. Stephens, R. L. Whetten, *Phys. Rev. Lett.* **1997**, *79*, 1873.
[36] C. Gautier, T. Bürgi, *Chem. Commun.* **2005**, 5393.
[37] S. Knoppe, N. Kothalawala, V. R. Jupally, A. Dass, T. Bürgi, *Chem. Commun.* **2012**, *48*, 4630.
[38] J. Zhang, Y. Zhou, K. Zheng, H. Abroshan, D. R. Kauffman, J. Sun, G. Li, *Nano Res.* **2018**, *11*, 5787.
[39] Y. Sato, M. Mitani, H. Yao, *J. Phys. Chem. C* **2020**, *124*, 25547.
[40] A. B. Buda, K. Mislow, *J. Am. Chem. Soc.* **1992**, *114*, 6006.
[41] Y. Yang, Q. Zhang, Z.-J. Guan, Z.-A. Nan, J.-Q. Wang, T. Jia, W.-W. Zhan, *Inorg. Chem.* **2019**, *58*, 3670.
[42] J.-H. Huang, X.-Y. Dong, Y.-J. Wang, S.-Q. Zang, *Coord. Chem. Rev.* **2022**, *470*, 214729.
[43] I. Dolamic, B. Varnholt, T. Bürgi, *Nat. Commun.* **2015**, *6*, 7117.
[44] I. Dolamic, S. Knoppe, A. Dass, T. Bürgi, *Nat. Commun.* **2012**, *3*, 798.
[45] C. Gautier, T. Bürgi, *J. Am. Chem. Soc.* **2008**, *130*, 7077.
[46] S. Malola, H. Häkkinen, *J. Am. Chem. Soc.* **2019**, *141*, 6006.
[47] X. Yang, L. Gan, L. Han, D. Li, J. Wang, E. Wang, *Chem. Commun.* **2013**, *49*, 2302.
[48] J. Liu, Y. Yu, C. Wang, J. Shen, J. Feng, W. Qi, *Chem. Commun.* **2021**, *57*, 10202.
[49] T. Mori, A. Sharma, T. Hegmann, *ACS Nano* **2016**, *10*, 1552.
[50] B. A. Rosales, M. P. Hanrahan, B. W. Boote, A. J. Rossini, E. A. Smith, J. Vela, *ACS Energy Lett.* **2017**, *2*, 906.
[51] S. González-Carrero, R. E. Galian, J. Pérez-Prieto, *Part. Part. Syst. Charact.* **2015**, *32*, 709.
[52] A. Dey, J. Ye, A. De, E. Debroye, S. K. Ha, E. Bladt, A. S. Kshirsagar, Z. Wang, J. Yin, Y. Wang, L. N. Quan, F. Yan, M. Gao, X. Li, J. Shamsi, T. Debnath, M. Cao, M. A. Scheel, S. Kumar, J. A. Steele, M. Gerhard, L. Chouhan, K. Xu, X. Wu, Y. Li, Y. Zhang, A. Dutta, C. Han, I. Vincon, A. L. Rogach, et al., *ACS Nano* **2021**, *15*, 10775.
[53] J. Jin, M. C. Folgueras, M. Gao, S. Yu, S. Louisia, Y. Zhang, L. N. Quan, C. Chen, R. Zhang, F. Seeler, K. Schierle-Arndt, P. Yang, *Nano Lett.* **2021**, *21*, 5415.
[54] G. Long, Y. Zhou, M. Zhang, R. Sabatini, A. Rasmita, L. Huang, G. Lakhwani, W. Gao, *Adv. Mater.* **2019**, *31*, 1807628.

[55] J. Ma, H. Wang, D. Li, *Adv. Mater.* **2021**, *33*, 2008785.
[56] T. He, J. Li, X. Li, C. Ren, Y. Luo, F. Zhao, R. Chen, X. Lin, J. Zhang, *Appl. Phys. Lett.* **2017**, *111*, 151102.
[57] W. Chen, S. Zhang, M. Zhou, T. Zhao, X. Qin, X. Liu, M. Liu, P. Duan, *J. Phys. Chem. Lett.* **2019**, *10*, 3290.
[58] D. G. Billing, A. Lemmerer, *Acta Crystallogr* **2003**, *59*, m381.
[59] C. U. Lee, S. Ma, J. Ahn, J. Kyhm, J. Tan, H. Lee, G. Jang, Y. S. Park, J. Yun, J. Lee, J. Son, J.-S. Park, J. Moon, *J. Am. Chem. Soc.* **2022**, *144*, 16020.
[60] H. Ren, Y. Wu, C. Wang, Y. Yan, *J. Phys. Chem. Lett.* **2021**, *12*, 2676.
[61] Y. Hu, F. Florio, Z. Chen, W. A. Phelan, M. A. Siegler, Z. Zhou, Y. Guo, R. Hawks, J. Jiang, J. Feng, L. Zhang, B. Wang, Y. Wang, D. Gall, E. F. Palermo, Z. Lu, X. Sun, T.-M. Lu, H. Zhou, Y. Ren, E. Wertz, R. Sundararaman, J. Shi, *Sci. Adv.* **2023**, *6*, eaay4213.
[62] J. Wang, H. Lu, X. Pan, J. Xu, H. Liu, X. Liu, D. R. Khanal, M. F. Toney, M. C. Beard, Z. V. Vardeny, *ACS Nano* **2021**, *15*, 588.
[63] B. Sepúlveda, P. C. Angelomé, L. M. Lechuga, L. M. Liz-Marzán, *Nano Today* **2009**, *4*, 244.
[64] L. M. Liz-Marzán, *Langmuir* **2006**, *22*, 32.
[65] S. Barbosa, A. Agrawal, L. Rodríguez-Lorenzo, I. Pastoriza-Santos, R. A. Alvarez-Puebla, A. Kornowski, H. Weller, L. M. Liz-Marzán, *Langmuir* **2010**, *26*, 14943.
[66] Z. Hu, D. Meng, F. Lin, X. Zhu, Z. Fang, X. Wu, *Adv. Opt. Mater.* **2019**, *7*, 1801590.
[67] I. Lieberman, G. Shemer, T. Fried, E. M. Kosower, G. Markovich, *Angew. Chem., Int. Ed.* **2008**, *47*, 4855.
[68] G. Zheng, S. Jiao, W. Zhang, S. Wang, Q. Zhang, L. Gu, W. Ye, J. Li, X. Ren, Z. Zhang, K. Wong, *Nano Res.* **2022**, *15*, 6574.
[69] Z. Fan, A. O. Govorov, *Nano Lett.* **2012**, *12*, 3283.
[70] H.-E. Lee, H.-Y. Ahn, J. Mun, Y. Y. Lee, M. Kim, N. H. Cho, K. Chang, W. S. Kim, J. Rho, K. T. Nam, *Nature* **2018**, *556*, 360.
[71] H. Kim, S. W. Im, N. H. Cho, D. H. Seo, R. M. Kim, Y.-C. Lim, H.-E. Lee, H.-Y. Ahn, K. T. Nam, *Angew. Chem., Int. Ed.* **2020**, *59*, 12976.
[72] H.-E. Lee, R. M. Kim, H.-Y. Ahn, Y. Y. Lee, G. H. Byun, S. W. Im, J. Mun, J. Rho, K. T. Nam, *Nat. Commun.* **2020**, *11*, 263.
[73] N.-N. Zhang, H.-R. Sun, Y. Xue, F. Peng, K. Liu, *J. Phys. Chem. C* **2021**, *125*, 10708.
[74] G. Zheng, J. He, V. Kumar, S. Wang, I. Pastoriza-Santos, J. Pérez-Juste, L. M. Liz-Marzán, K.-Y. Wong, *Chem. Soc. Rev.* **2021**, *50*, 3738.
[75] C. Gautier, T. Bürgi, *ChemPhysChem* **2009**, *10*, 483.
[76] T. Hegmann, H. Qi, V. M. Marx, *J. Inorg. Organomet. Polym. Mater.* **2007**, *17*, 483.
[77] M. Bagiński, M. Tupikowska, G. González-Rubio, M. Wójcik, W. Lewandowski, *Adv. Mater.* **2020**, *32*, 1904581.
[78] K. Morisawa, T. Ishida, T. Tatsuma, *ACS Nano* **2020**, *14*, 3603.
[79] K. Hou, J. Zhao, H. Wang, B. Li, K. Li, X. Shi, K. Wan, J. Ai, J. Lv, D. Wang, Q. Huang, H. Wang, Q. Cao, S. Liu, Z. Tang, *Nat. Commun.* **2020**, *11*, 4790.
[80] X. Zhu, J. Zhang, J. Liu, Y. Zhang, *Adv. Sci.* **2019**, *6*, 1901358.
[81] B. Chen, F. Wang, *Trends Chem.* **2020**, *2*, 427.
[82] J. Ferrera-González, L. Francés-Soriano, C. Galiana-Roselló, J. González-Garcia, M. González-Béjar, E. Fröhlich, J. Pérez-Prieto, *Biomedicines* **2021**, *9*, 1419.
[83] Y. Zhang, X. Zhu, Y. Zhang, *ACS Nano* **2021**, *15*, 3709.
[84] Y.-H. Chien, K. K. Chan, S. H. K. Yap, K.-T. Yong, *J. Chem. Technol. Biotechnol.* **2018**, *93*, 1519.
[85] R. Rafique, S. K. Kailasa, T. J. Park, *Trends Analyt Chem* **2019**, *120*, 115646.
[86] B. Gu, Q. Zhang, *Adv. Sci.* **2018**, *5*, 1700609.
[87] Z. Li, H. Yuan, W. Yuan, Q. Su, F. Li, *Coord. Chem. Rev.* **2018**, *354*, 155.
[88] M. S. Arai, A. S. S. de Camargo, *Nanoscale Adv* **2021**, *3*, 5135.
[89] B.-T. Liu, T.-H. Huang, T.-L. Wang, C.-C. Hsu, *Sol. Energy* **2021**, *227*, 1.
[90] J. Jiang, H. Ren, F. Huang, L. Wang, J. Zhang, *CrystEngComm* **2021**, *23*, 6117.
[91] Y. Liu, S. Liang, C. Yuan, A. Best, M. Kappl, K. Koynov, H.-J. Butt, S. Wu, *Adv. Funct. Mater.* **2021**, *31*, 2103908.
[92] W. Ma, H. Kuang, L. Wang, L. Xu, W.-S. Chang, H. Zhang, M. Sun, Y. Zhu, Y. Zhao, L. Liu, C. Xu, S. Link, N. A. Kotov, *Sci. Rep.* **2013**, *3*, 1934.
[93] S. Ostovar pour, L. Rocks, K. Faulds, D. Graham, V. Parchaňský, P. Bouř, E. W. Blanch, *Nat. Chem.* **2015**, *7*, 591.
[94] X. Wu, L. Xu, W. Ma, L. Liu, H. Kuang, N. A. Kotov, C. Xu, *Adv. Mater.* **2016**, *28*, 5907.
[95] J. Dong, W. Gao, Q. Han, Y. Wang, J. Qi, X. Yan, M. Sun, *Rev. Phys.* **2019**, *4*, 100026.
[96] S. Li, L. Xu, W. Ma, X. Wu, M. Sun, H. Kuang, L. Wang, N. A. Kotov, C. Xu, *J. Am. Chem. Soc.* **2016**, *138*, 306.
[97] C. Hao, X. Wu, M. Sun, H. Zhang, A. Yuan, L. Xu, C. Xu, H. Kuang, *J. Am. Chem. Soc.* **2019**, *141*, 19373.
[98] T.-D. Nguyen, W. Y. Hamad, M. J. MacLachlan, *Adv. Opt. Mater.* **2017**, *5*, 1600514.
[99] X. Jin, Y. Sang, Y. Shi, Y. Li, X. Zhu, P. Duan, M. Liu, *ACS Nano* **2019**, *13*, 2804.
[100] X. Zhu, Y. Li, P. Duan, M. Liu, *Chem. – A Eur. J.* **2010**, *16*, 8034.
[101] Y. Xie, Z. Feng, C. Zhang, X. Tang, F. Lu, X. Wang, H. Zhang, C. He, J. Li, Y. Huang, D. Zhang, X. Chen, G. Zou, *ACS Appl. Nano Mater.* **2021**, *4*, 5285.
[102] A. Juan, H. Sun, J. Qiao, J. Guo, *Chem. Commun.* **2020**, *56*, 13649.
[103] Q. Shao, G. Zhang, L. Ouyang, Y. Hu, Y. Dong, J. Jiang, *Nanoscale* **2017**, *9*, 12132.
[104] H. He, M. Cen, J. Wang, Y. Xu, J. Liu, W. Cai, D. Kong, K. Li, D. Luo, T. Cao, Y. Jun Liu, *ACS Appl. Mater. Interfaces* **2022**, *14*, 53981.
[105] M. Zhou, Y. Sang, X. Jin, S. Chen, J. Guo, P. Duan, M. Liu, *ACS Nano* **2021**, *15*, 2753.
[106] W. Li, M. Xu, C. Ma, Y. Liu, J. Zhou, Z. Chen, Y. Wang, H. Yu, J. Li, S. Liu, *ACS Appl. Mater. Interfaces* **2019**, *11*, 23512.
[107] X. Yang, M. Zhou, Y. Wang, P. Duan, *Adv. Mater.* **2020**, *32*, 2000820.
[108] X. Jin, M. Zhou, J. Han, B. Li, T. Zhang, S. Jiang, P. Duan, *Nano Res.* **2022**, *15*, 1047.
[109] A. Bobrovsky, K. Mochalov, V. Oleinikov, A. Sukhanova, A. Prudnikau, M. Artemyev, V. Shibaev, I. Nabiev, *Adv. Mater.* **2012**, *24*, 6216.
[110] S. Zhang, Y. Wang, F. Meng, C. Dai, Y. Cheng, C. Zhu, *Chem. Commun.* **2015**, *51*, 9014.
[111] D. Yang, P. Duan, L. Zhang, M. Liu, *Nat. Commun.* **2017**, *8*, 15727.
[112] J. Wade, J. R. Brandt, D. Reger, F. Zinna, K. Y. Amsharov, N. Jux, D. L. Andrews, M. J. Fuchter, *Angew. Chem., Int. Ed.* **2021**, *60*, 222.
[113] T. Nishikawa, Y. Nagata, M. Suginome, *ACS Macro Lett.* **2017**, *6*, 431.
[114] Z. Fan, A. O. Govorov, *Nano Lett.* **2010**, *10*, 2580.
[115] D. Li, X. Liu, W. Wu, Y. Peng, S. Zhao, L. Li, M. Hong, J. Luo, *Angew. Chem., Int. Ed.* **2021**, *60*, 8415.

Laura Francés-Soriano is a Distinguished Researcher at the Institut de Ciència Molecular (ICMOL), Universitat de València. She obtained her Ph.D. in chemistry from the University de València in 2017. She was a Marie Sklodowska-Curie Individual Fellow in the CNRS (France), where she worked in FRET-based biosensing and bioimaging. Her present research is focused on the rational design and fabrication of upconversion-based probes for bioimaging.

MElena Zaballos García, is a full professor in the Department of Organic Chemistry of the University of Valencia (Spain). She teaches different subjects in the Department of Organic Chemistry of the University of Valencia, including Chemical Engineering, Industrial Electronic Engineering, Optics, Pharmacy, Chemistry, Human Nutrition and Dietetics, Biological Sciences and Biotechnology. Her main research interests include the synthesis and studies in the area of heterocyclic chemistry, asymmetric synthesis, photochemistry, studies of reaction mechanisms, synthesis and functionalization of nanostructures, in particular gold nanoparticles and nanoclusters, and study of their interaction with drugs, and the possible applications such as sensing and bioimaging

Julia Pérez-Prieto has been a professor at the University of Valencia since 2007. She is the leader of the Photochemical Reactivity Group at the Institute of Molecular Science of the University of Valencia. Her research interests are currently focused on the design and synthesis of new photoactive nanomaterials, such as lead halide perovskites, gold nanoparticles and gold nanoclusters, upconversion nanoparticles and hybrid nanomaterials, as well as lanthanide complexes, to address major challenges in sensing, imaging, therapy, and sustainability. Julia Pérez-Prieto has made significant contributions to the area of synthesis, catalysis, photochemistry, and photoactive nanomaterials.